Temporal and spatial structure of nocturnal warming events in a midlatitude coastal city

Isabelle Renee Lao, Carsten Abraham, Ed Wiebe, and Adam H. Monahan

2022

Original citation:
Lao, I. R., Abraham, C., Wiebe, E., & Monahan, A. H. (2022). Temporal and spatial structure of nocturnal warming events in a midlatitude coastal city. *Journal of Applied Meteorology and Climatology*, *61*(9), 1139–1157. https://doi.org/10.1175/jamc-d-21-0205.1

Temporal and Spatial Structure of Nocturnal Warming Events in a Midlatitude Coastal City

ISABELLE RENEE LAO,[a] CARSTEN ABRAHAM,[a,b] ED WIEBE,[a] AND ADAM H. MONAHAN[a]

[a] *School of Earth and Ocean Sciences, University of Victoria, Victoria, British Columbia, Canada*
[b] *Canadian Centre for Climate Modelling and Analysis, Environment and Climate Change Canada, Victoria, British Columbia, Canada*

(Manuscript received 4 October 2021, in final form 5 May 2022)

ABSTRACT: Nocturnal warming events (NWEs) are abrupt interruptions in the typical cooling of surface temperatures at night. Using temperature time series from the high-resolution Vancouver Island School-Based Weather Station Network (VWSN) in British Columbia, Canada, we investigate temporal and spatial characteristics of NWEs. In this coastal region, NWEs are more frequently detected in winter than in summer, with a seasonal shift from slowly warming NWEs dominating the winter months to rapidly warming NWEs dominating the summer months. Slow-warming NWEs are of relatively small amplitude and exhibit slow cooling rates after the temperature peaks. In contrast, fast-warming NWEs have a temperature increase of several kelvins with shorter-duration temperature peaks. The median behavior of these distinct NWE classes at individual stations is similar across the entire set of stations. The spatial synchronicity of NWEs across the VWSN (determined by requiring NWEs at station pairs to occur within given time windows) decreases with distance, including substantial variability at nearby stations that reflects local influences. Fast-warming NWEs are observed to occur either simultaneously across a number of stations or in isolation at one station. Spatial synchronicity values are used to construct undirected networks to investigate spatial connectivity structures of NWEs. We find that, independent of individual seasons or NWE classes, the networks are largely unstructured, with no clear spatial connectivity structures related to local topography or direction.

KEYWORDS: Atmosphere; Coastlines; Complex terrain; North America; Boundary layer; Climate classification/regimes; Coastal meteorology; Surface temperature

1. Introduction

The nocturnal boundary layer (NBL) typically begins to form in the late evening hours when shortwave radiation fluxes weaken and longwave radiative cooling dominates the surface energy budget (e.g., Acevedo and Fitzjarrald 2001; Ha and Mahrt 2003; Edwards 2009a,b; van Hooijdonk et al. 2017). As a result, near-surface atmospheric layers tend to cool in the NBL, often resulting in the development of shallow temperature inversions and a stably stratified boundary layer (SBL, e.g., Mahrt 2014; van Hooijdonk et al. 2017; Abraham and Monahan 2019b,c; Acevedo et al. 2019; Maroneze et al. 2019, 2021). NBL mean and turbulence structures are considerably more variable in space and time than the typical daytime convective boundary layer and are governed by different processes (e.g., Acevedo and Fitzjarrald 2001, 2003; Coulter and Doran 2002; Mahrt et al. 2009, 2020, 2021; Mahrt 2014; Sun et al. 2002, 2004, 2015a,b; Mortarini et al. 2016, 2019; Cava et al. 2017, 2019). Because of a lack of long-term measurement sites with high spatial and temporal resolution, little is known about the spatial variability of NBL structures and processes. Nocturnal warming events (NWEs) are a useful phenomenon in understanding the spatial and temporal structures of different processes producing NBL variability. In qualitative terms, we define NWEs as relatively strong near-surface temperature increases interrupting the typical radiative cooling in the NBL (a more precise quantitative definition is provided later). In this study, we use data from a long-term measurement network of approximately 100 stations to quantify the occurrence frequency as well as temporal and spatial structures of NWEs in the greater Victoria region of British Columbia, Canada.

NWEs can be associated with different phenomena, of which the best understood are synoptic-scale meteorological changes such as frontal passages (Smith et al. 1995; Sanders and Kessler 1999; Nallapareddy et al. 2011; Hu et al. 2013), warm-air advection (Mahrt 2017), and changing cloud cover influencing the longwave radiation budget at the surface (Abraham and Monahan 2019b). NWEs that can be associated with such events are generally well understood, and their origins and impacts on NBL structures are clear. Another class of NWEs can be associated with relatively small-scale phenomena such as intermittent turbulence events under conditions of very strong stable stratification.

The stable boundary layer is often classified into two regimes: weakly stable (wSBL) and very stable (vSBL; e.g., Mahrt 1998, 2014; Mahrt et al. 2013, 2015; Acevedo and Fitzjarrald 2003; Bonin et al. 2015; van Hooijdonk et al. 2015; Monahan et al. 2015; Acevedo et al. 2016, 2019; Vignon et al. 2017; Abraham and Monahan 2019a,b,c). The wSBL is governed by sustained downward turbulent energy transport almost balancing the radiative flux divergence at the surface, such that cooling rates of near-surface atmospheric layers are weak. In contrast, the vSBL is governed by weak to collapsed turbulence that cannot balance surface longwave radiative energy loss, causing large cooling rates and strong near-surface inversions. A phenomenon particular to the vSBL is the occurrence of intermittent turbulence events that accompany

---

Corresponding authors: Isabelle Renee Lao, lao.isabelle@gmail.com; Carsten Abraham, carsten.abraham@ec.gc.ca

DOI: 10.1175/JAMC-D-21-0205.1

abrupt NWEs (e.g., Nappo 1991; Acevedo and Fitzjarrald 2001, 2003; Coulter and Doran 2002; Sun et al. 2002, 2004, 2012, 2015a,b; White 2009; Deb Burman et al. 2018; Abraham and Monahan 2020).

Intermittent turbulence events can result from interactions of submesoscale motions (atmospheric motions that are larger than turbulence but smaller than the mesoscale) with turbulence, which can locally mix warmer air and momentum from aloft toward the surface (e.g., Nappo 1991; Sun et al. 2002, 2004, 2015a,b; Coulter and Doran 2002; Reina and Mahrt 2005; White 2009; Acevedo et al. 2014; Mahrt 2014, 2019; Kang et al. 2015; Cava et al. 2019; Deb Burman et al. 2018; Petenko et al. 2019; Abraham and Monahan 2020). Such events arise from submesoscale phenomena ranging over many different time (from minutes to hours) and spatial scales (from meters to tens of kilometers) (e.g., Sun et al. 2004; Mahrt 2010, 2014; Mahrt et al. 2009, 2020, 2021; Hoover et al. 2015; Thomas 2011; Thomas et al. 2012; Zeeman et al. 2015; Vercauteren and Klein 2015; Vercauteren et al. 2016; Boyko and Vercauteren 2021). NWEs that are caused by intermittent turbulence events are often, but not necessarily, associated with the occurrence of rapid regime transitions in the SBL (e.g., Acevedo and Fitzjarrald 2001; Van de Wiel et al. 2002, 2003; Abraham et al. 2019). The drivers of such intermittent turbulence events, their spatial structures, and the structures of their accompanied NWEs are not well understood (Thomas 2011; Acevedo et al. 2014; Zeeman et al. 2015; van Hooijdonk et al. 2015; Vercauteren and Klein 2015; Vercauteren et al. 2016; Mahrt et al. 2020; Sun et al. 2015b; Abraham and Monahan 2019b).

A number of case studies across a range of locations have identified NWEs, wherein the steady nocturnal cooling phase is suddenly interrupted by large temperature increases (e.g., Coulter and Doran 2002; Sun et al. 2002, 2004; White 2009; Nallapareddy et al. 2011; Hu et al. 2013; Ma et al. 2015; Deb Burman et al. 2018). Many of these studies found that the NWEs were caused by intermittent turbulence events occurring under weak wind conditions, strong stratification, and weak background turbulence intensities, all of which are very typical in vSBL conditions. The NWEs are then accompanied by large increases in wind speeds and turbulence intensity, confirming the idea of a sudden onset of vertical turbulent mixing transporting warmer air masses with more momentum from aloft toward the surface. Case studies, however, do not allow for the quantification of climatological features. Additionally, single observational sites do not allow for the quantification of the spatial structures of such NWEs.

For the most part, the lack of capable observational systems has been an obstacle hindering substantial advances in characterizing spatial structures of NWEs. Although some new measurement techniques have the potential to fill this gap (Mahrt et al. 2020; Lapo et al. 2021; Pfister et al. 2021a,b), the measurement domains are still smaller than some observed NWE structures likely associated with intermittent turbulence events and synchronous SBL regime transitions that can span tens of kilometers (e.g., Coulter and Doran 2002; Medeiros and Fitzjarrald 2014, 2015; Abraham and Monahan 2020). In addition to improving the physical understanding of the spatial structures of NWEs, a better understanding of their nature and occurrence frequency provides useful information for improving the representation of the SBL in models for weather and climate (Holtslag et al. 2013; Mahrt 2014; Maroneze et al. 2021; Abraham et al. 2019).

In this study, we investigate the climatological characteristics of NWEs within the Vancouver Island School-Based Weather Station Network (VWSN) in the greater Victoria region (Fig. 1). The VWSN is of relatively large spatial extent and high spatial resolution (tens of kilometers and less than ~1 km, respectively). The mostly school-based VWSN consists of commercial weather stations and was originally designed for the purpose of community education. As such, station instrumentation and siting do not accord with standards of the World Meteorological Organization (WMO), and the spatial distribution is not uniform. Nonetheless, we find that the data allow for the identification of NWEs and quantification of their climatological temporal and spatial structures. While our analysis does not allow us to unambiguously distinguish NWEs caused by different mechanisms (e.g., synoptic-scale processes vs local intermittent turbulence), we do find robust differences in temporal and spatial structures between different classes of NWEs.

Representative examples of NWEs occurring in the greater Victoria region are shown in Fig. 1. We identify many abrupt NWEs, similar to those in the case studies mentioned above, in which the steady nocturnal cooling rate is suddenly interrupted by a temperature increase of a few kelvins. The temperature peak is then followed by a cooling phase where the temperature tendency returns to the radiative cooling background state [e.g., University of Victoria (UVic) Ian-Stewart Complex (ISC), 26–27 August 2019]. Such NWEs are consistent with transient warming resulting from an intermittent turbulence event. Other identified NWEs show clear characteristics of large-scale forcings, such as abrupt warming followed by a new atmospheric state that is sustained for several hours (e.g., Sidney, 13–14 June 2006). These types of events are consistent with the passing of a frontal system or the advection of a different air mass. Some nights exhibit several NWEs with a typical temperature spike (e.g., Happy Valley, 11–12 September 2013). However, not all detected NWEs demonstrate such a clear, isolated structure, with many emerging from a more chaotic background state in which cooling and warming phases alternate frequently (e.g., James Bay, 28–29 August 2013). These complex NWE sequences could be associated with alternating periods of cloud cover and clear sky.

The long duration, broad spatial extent, and relatively high space–time resolution of the VWSN dataset allow us to study the climatological occurrence frequency, temporal structure, and spatial structures of NWE in unprecedented detail across the greater Victoria region. This study first provides an overview of the data considered (section 2), followed by descriptions of the NWE detection algorithm and the network analysis technique to identify spatial dependencies (section 3). Results are presented in section 4, followed by a discussion and conclusions in section 5.

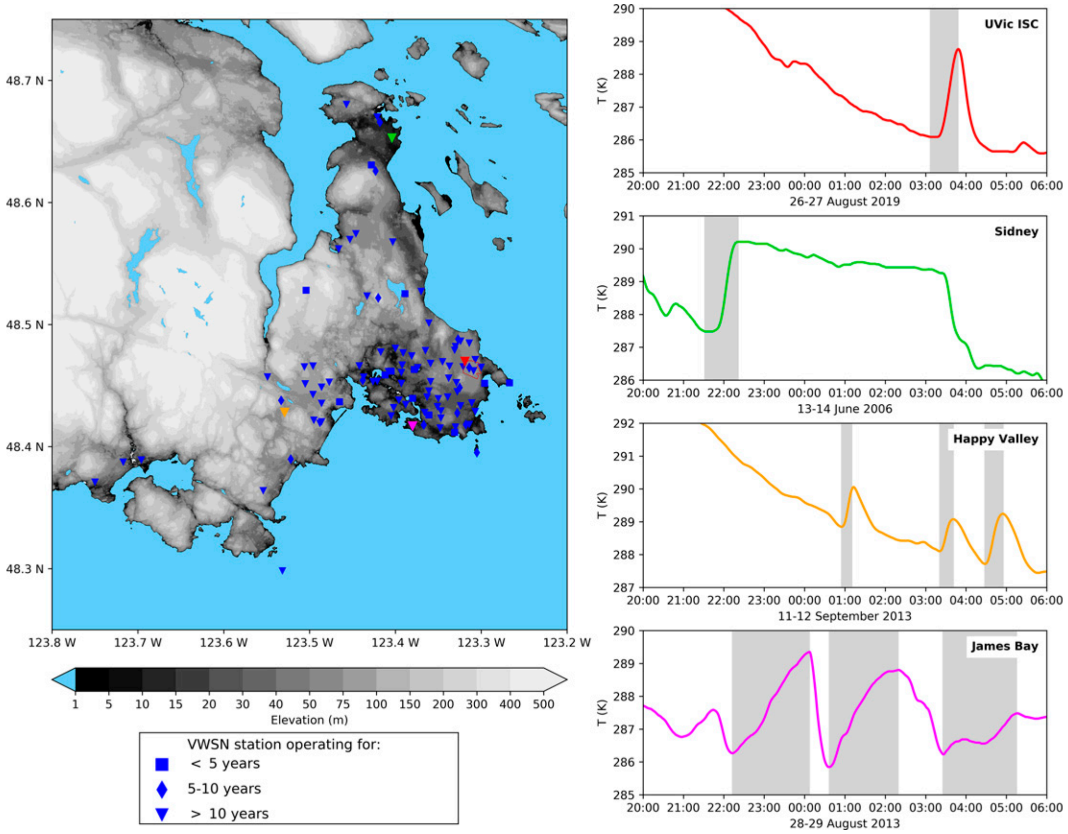

FIG. 1. (left) Topography of the greater Victoria region and the locations of 99 of 101 VWSN stations (two stations lie outside the map domain). The University of Victoria campus is demarcated by the brown line beside the red symbol. (right) Temperature time series of representative NWEs (warming phases shaded in gray), with line colors corresponding to the station colors on the map. The topographic data are provided by the Japan Aerospace Exploration Agency through the Advanced Land Observing Satellite Global Digital Surface Model.

2. Datasets

a. VWSN

The VWSN consists of Davis Vantage Pro 2 weather stations located on Vancouver Island, British Columbia, Canada. Most of the stations are in the Capital Regional District (greater Victoria), a medium-sized urban area on the Pacific coast (~48.5°N, 123.4°W; Fig. 1). The VWSN collects, stores, processes, and displays near-surface meteorological observations primarily for educational purposes. The measuring instruments are mostly on school buildings to take advantage of power and Internet access and for measurement site security. The VWSN developed over several years: the first station was installed in 2002 at the University of Victoria (UVic ISC; red symbol on the map in Fig. 1), and the first larger-scale installation of 20 stations occurred in 2005. By 2006, there were 67 sites spread across the greater Victoria area. Since then, stations have been added in different regions to a total of 150 sites all over Vancouver Island as of January 2021. The majority of stations have been reliably operating over this time period, but occasional failures of instruments or changes to the station sites resulted in intermittent outages. Because of limited resources, some locations with recurring failures were abandoned. For our analysis, we use data collected from 11 March 2002 to 12 September 2019 from approximately 100 stations across the greater Victoria area. Although we do not have continuous measurements at all 100 stations, on any given night, data from about 80% of those VWSN stations are available. Nights at a single station with unphysical temperature spikes and data gaps are removed entirely. Because the NBL conditions are in good approximation independent of the conditions of a previous night (Blay-Carreras et al. 2014), the removal of nights or occasional outages at a station do not affect our analysis of studying climatological occurrence frequencies and structures of NWE, particularly over the long duration of the observation period.

School buildings, where measuring instruments are placed, vary in design. Many are low, flat-roofed structures, usually surrounded by expansive open areas and grassy parkland. They are typically installed near the roof edge with an elevation higher than or equal to 1.5 m from the roof top. The structures supporting the instruments are covered in typical roofing materials, such as asphalt shingle, steel, and gravel covered or bare roll-on surfaces. While the VWSN stations do not comply to WMO standards for measuring near surface meteorological variables, the pressure and temperature measurements have been shown to be in good agreement with WMO standard measurements from Environment and Climate Change Canada (ECCC) measurements (Rabinovich et al. 2020; Evins et al. 2020).

Each weather station measures air temperature, relative humidity, insolation, wind speed, wind direction, and atmospheric pressure, of which we only use the temperature measurement in our analysis. The temperature sensor is a shielded PN junction silicon diode with a resolution of 0.1 ± 0.3 K. Other instrument specifications are available from Davis Instruments (https://davisnet.com/). Observations are read from each station continuously, with updates every 2–3 s, and are finally averaged over 1-min intervals. All observations are stored and published on the VWSN website (https://victoriaweather.ca/). A detailed discussion of the VWSN is presented in Weaver and Wiebe (2006).

b. *Comparison of VWSN with ECCC temperature observations*

UVic is also home to one ECCC station (48.457°N, 123.30461°W; Fig. 2) that measures temperatures according to WMO standards. The ECCC station is placed in an open field on a relatively homogeneous plateau about 60 m above sea level. About 40 m south of the ECCC station remain about 40 trees from an old orchard. About 300 m northwest of the ECCC station is a forested narrow creek valley that separates the station from the UVic main campus (Fig. 2, brown ellipse in map).

Temperature measurements at the ECCC station are provided as hourly means. The measurements are taken 1.5 m above ground and have an accuracy of 0.1 K. Although the relatively coarse temporal resolution of the ECCC data does not allow for studying NWEs, it does provide a valuable point of comparison for the VWSN data.

As a simple quality assessment of the VWSN data, hourly mean nocturnal temperature measurements of the six closest VWSN stations on and around the UVic campus (of distance between 650 and 1800 m from the ECCC station; Fig. 2, top-left panel) are used to compare VWSN temperature measurements with the WMO standard ECCC station observations. For this and subsequent analyses, VWSN data are corrected for daylight saving time and moved to coordinated universal time. We further define nighttime as the time between sunset and sunrise calculated from the date and geographical location through the sunrise function from the MathWorks library. While ECCC operates several stations in and around Victoria, the topographic setting of the UVic campus and its surroundings is well suited to assess systematic differences between the Davis Vantage Pro 2 instruments on school buildings and WMO standard measurements. The topographic complexity of southern Vancouver Island (cf. Fig. 1) and the distance to other ECCC stations make such a comparison in other parts of the greater Victoria region less meaningful.

The probability density functions (pdfs) of the hourly mean temperature differences between the VWSN and ECCC stations are similar across the six stations considered (Fig. 2, top right). Although the pdfs are positively skewed, the mean temperature differences across all stations are less than about 1 K. The mean difference increases systematically with the installation height of the instruments, with the elevation being constrained by the building structures. The lowest mean difference (0.2 K) is observed at Campus View, a one-story school building with a flat roof, whereas UVic Bob-Wright Centre Building (BWC) and UVic David Turpin Building (DTB), the stations with the largest mean temperature differences (1.2 and 1 K, respectively), are five-story buildings. Because the NBL is often dominated by radiative cooling at the surface causing warmer temperatures aloft, the positive mean and skewness of the temperature difference pdfs are not surprising.

The joint pdfs of the hourly mean temperature measurements at the ECCC station and each individual VWSN station further demonstrate the strong correlation between the temperature observations (Fig. 2, lower panels). Again, in comparison with the observations on top of the three taller UVic buildings, slightly larger correlations at the three school buildings are found (Arbutus, Campus View, and Frank Hobbs).

NWEs, by definition, involve temperature changes and not the actual temperature values, so any small systematic differences of temperature measurements between stations should not materially affect the NWE analyses. In general, the comparison of the VWSN and WMO station observations indicates the reliability of the VWSN temperature data for this analysis.

3. Methods

a. *Nocturnal warming event detection*

The NWEs are detected from the 1-min-averaged nocturnal temperature time series. To improve the signal-to-noise ratio in the time series, a centered 11-min running mean is first applied. Based on our NWE detection method, the shortest NWEs have a warming phase (from beginning of NWE to the temperature maximum) of about 20 min. This duration is sufficiently long relative to the 11-min time averaging that small, high-frequency fluctuations are filtered out while lower-frequency warming phases are retained.

Because NWEs usually exhibit local temperature maxima, we use the MATLAB findpeaks function as the preliminary detection tool. This function is particularly useful for detecting NWEs because it identifies local maxima on the basis of their prominence, a metric characterizing the strength of a peak relative to nearby features in the time series. The prominence is defined as the difference between the signal value of a local maximum (such as an NWE temperature peak) and the larger absolute value of the two global minima on either side of the local maximum (Fig. 3a; blue arrows). The intervals span either from the signal peak to the next or previous time the signal again is equal to the value of the peak (e.g., the left interval in Fig. 3a), or, if the peak is the global maximum of the interval, from the peak to the signal start or end (e.g., the right interval in Fig. 3a). In the example of Fig. 3a the identified prominence of the NWE is indicated by the blue arrow in the left interval.

Having identified temperature peaks, a set of criteria is used to identify NWEs of interest. These criteria are developed

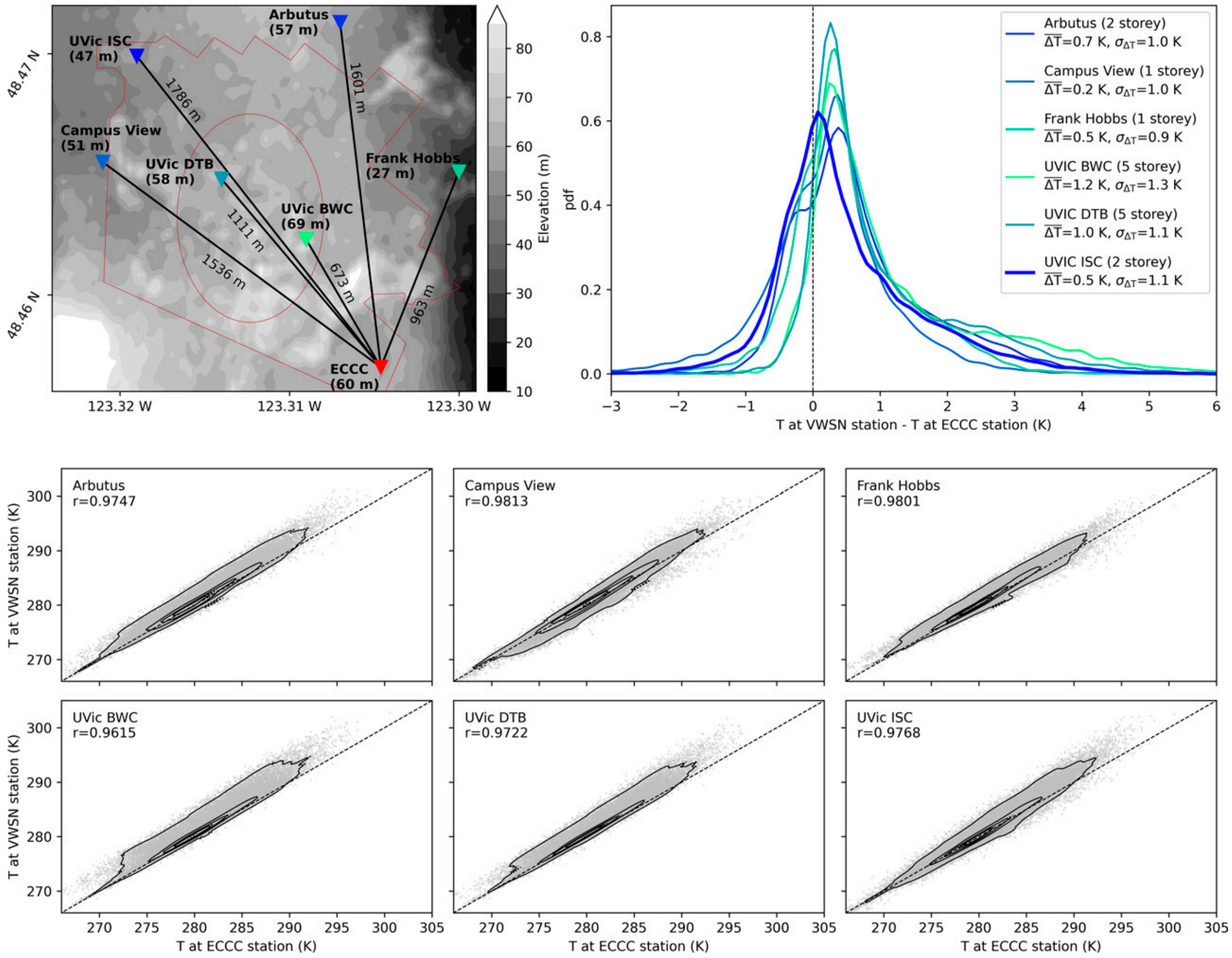

FIG. 2. (top left) Comparison of temperature measurements between the UVic ECCC station (red symbol) and the six closest VWSN stations on and around the UVic Campus (brown lines; the ellipse indicates the main campus with the tallest buildings): Arbutus Global Middle School, Campus View Elementary School, Frank Hobbs Elementary School, UVic BWC, UVic DTB, and UVic ISC. The instrument measurement heights at these stations and their distances to the UVic ECCC station are indicated in the top-left panel, and the building heights on which the instruments are mounted are provided in the legend of the top-right panel. (top right) Pdf of the nighttime (from sunset to sunrise) hourly mean temperature differences between the six VWSN stations and UVic ECCC for time periods from June 2006 (Arbutus), May 2005 (Campus View), June 2005 (Frank Hobbs), April 2009 (UVic BWC), May 2010 (UVic DTB), and April 2002 (UVic ISC) to August 2019. The time-period differences result from differing instrument installation dates at each station. (bottom) Scatterplots of the temperature measurements at ECCC against the VWSN stations (gray dots). Black contours illustrate estimates of the bivariate joint pdf; these are compared with the black dotted 1:1 lines (actual correlations are stated in the top left of each panel). All pdfs are calculated with the multivariate kernel density estimation of O'Brien et al. (2014, 2016). The topographic data are as in Fig. 1.

through consideration of temperature time series from a randomly selected subset of nights, in which NWEs can be identified through visual inspection. Parameter values in the detection algorithm are set to ensure a low rate of both false positive and false negative NWE detections. We find that the detection of NWEs through this algorithm has a relatively low sensitivity to small deviations from the final parameter values such that qualitatively similar conclusions can be drawn. However, the parameters might be only applicable to this dataset and further investigations for a generalization of the algorithm to other locations is required.

We only consider NWEs with a minimum temperature increase of 1 K and consistent warming rates (from event onset to peak) greater than 0.4 K h^{-1}. These criteria were chosen to focus the analysis on relatively pronounced NWEs, rather than small temperature fluctuations. The detection algorithm identifies the NWE start time t_s and peak time t_p as follows (with T denoting temperature in kelvins):

1) The T peaks are identified at t_p if their prominence is at least 0.8 K (Fig. 3a). The prominence threshold of 0.8 K was chosen because a number of NWEs, identified by eye, exhibit a warming of about 1 K but subsequent temperature decreases smaller than 1 K. Such events result in prominence values smaller than 1 K (cf. definition above).

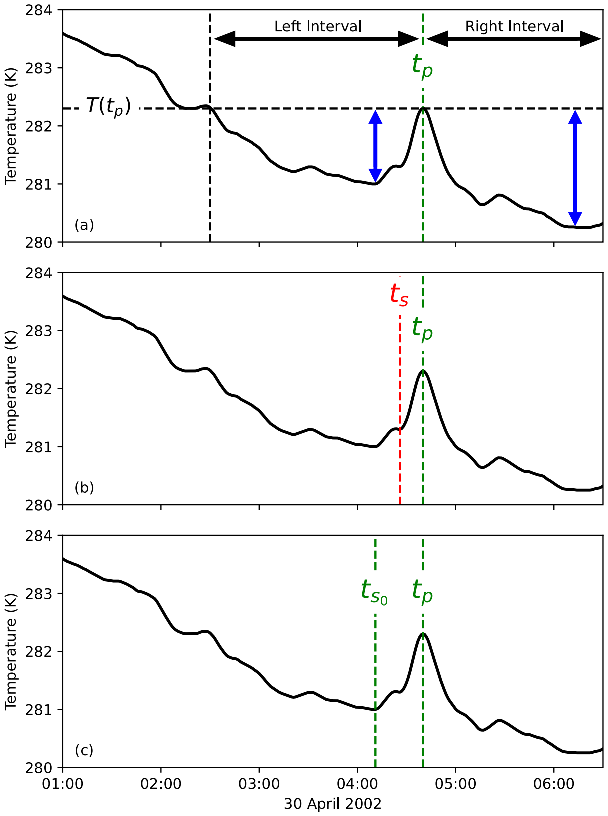

FIG. 3. Illustration of the definition of the temperature time series prominence [in (a)] and the NWE detection algorithm steps (a) 1, (b) 2, and (c) 3 by means of a representative NWE from the night of 29 Apr 2002 at the UVic ISC station. The time t_p (temperature peak of the NWE) defines one of the boundaries of the two search intervals [black arrows in (a)] to identify the prominence [blue arrows in (a)] of the NWE. The algorithm then determines a provisional event start time t_s [red line in (b)] followed by a second estimate t_{s_0} [in (c)]. This second estimate is determined by the algorithm to be the "true" event start time.

2) The nearest T minimum preceding the local T peak at $t_s < t_p$, is identified (Fig. 3b, red line).
3) To ensure that the event start time t_s is not incorrectly identified because of a small positive fluctuation in $T(t_s)$ (as is the case for the local minimum indicated in Fig. 3b), the nearest local minimum (at t_{s_0}) and local maximum (at t_{s_m}) preceding t_s are identified (such that $t_{s_0} < t_{s_m} < t_s$). If no preceding local maximum is identified between the start of the night and time t_s, then t_s is retained and the algorithm continues in step 4; otherwise
   (i) if $T(t_{s_m}) - T(t_s) \leq 0.2$ K and $T(t_{s_0}) - T(t_s) < 0$ K, t_s is considered to be part of a small temperature fluctuation within the NWE. The event start time t_s is replaced by the value of t_{s_0} (left green line in Fig. 3c) and the algorithm returns to step 2;
   (ii) if $T(t_{s_m}) - T(t_s) > 0.2$ K or $T(t_{s_0}) - T(t_s) \geq 0$ K, the start time t_s is retained and the algorithm proceeds to step 4.
4) To ensure that $\partial T/\partial t > 0.4$ K h^{-1} is consistently maintained across the warming phase of the NWE, a moving regression line is fit in 30-min sliding windows from t_p backward to t_s. The value of t_s is retained if all estimated regression line slopes are larger than 0.4 K h^{-1} or set to the time at which the regression line slope is first less than 0.4 K h^{-1}.
5) Last, the peak is identified as an NWE if $T(t_p) - T(t_s) \geq 1$ K.

The results of our analysis are not qualitatively sensitive to moderate changes in the parameters used in this NWE detection algorithm.

b. *Event synchronization and network analysis*

To investigate the spatial extent of NWEs and their connectivity structure across the VWSN, we use a combination of event synchronization (ES) and network analysis. ES is a simple, symmetric measure of joint occurrence of events defined in two time series, $x(t)$ and $y(t)$. Denoting individual events in $x(t)$ and $y(t)$ respectively as t_{x_l} and t_{y_m}, with $l \in L = \{1, 2, \ldots, S_x\}$ and $m \in M = \{1, 2, \ldots, S_y\}$, the ES measure quantifies the number of synchronously occurring events C and assigns an event synchronization strength Q (Quian Quiroga et al. 2002). By construction, $Q \in [0, 1]$, with $Q = 1$ indicating perfect event synchronicity and $Q = 0$ indicating no event synchronicity at all. In our analysis, time series $x(t)$ and $y(t)$ consist of all concatenated nights for a given pair of two stations measured continuously. In the context of ES analysis, events are defined as occurring "synchronously" across the two time series if they occur within a specified, finite time window, $\tau \geq |t_{x_l} - t_{y_m}| \geq 0$. The definition of C is

$$C = \sum_{l=1}^{S_x} J(l, m_l), \tag{1}$$

where

$$J(l, m) = \begin{cases} 1, & 0 \leq |t_{x_l} - t_{y_m}| \leq \tau \\ 0, & \text{otherwise} \end{cases}, \tag{2}$$

and m_l is the index value of the event in y_m closest in time to the event peak time t_{x_l}. To avoid double counting of events, m_l is only taken from the subset of events $M \backslash K_l$, where the excluded subset $K_l \subseteq M$ consists of all m_k for which $J(k, m_k) = 1$ with $1 < k < l$ (i.e., the set of events in y that are determined to be synchronous with an event in x before t_{x_l}). Last, Q is given by

$$Q = \frac{C}{\sqrt{S_x S_y}}. \tag{3}$$

The relatively simple definition of C differs from those used in previous studies (e.g., Malik et al. 2010, 2012; Rheinwalt et al. 2012, 2016; Agarwal et al. 2017; Conticello et al. 2018, 2020; Boers et al. 2013; Cheung and Ozturk 2020) in that it allows investigation of spatial connectivity structures but does not provide information about propagation direction. The use of a more sophisticated

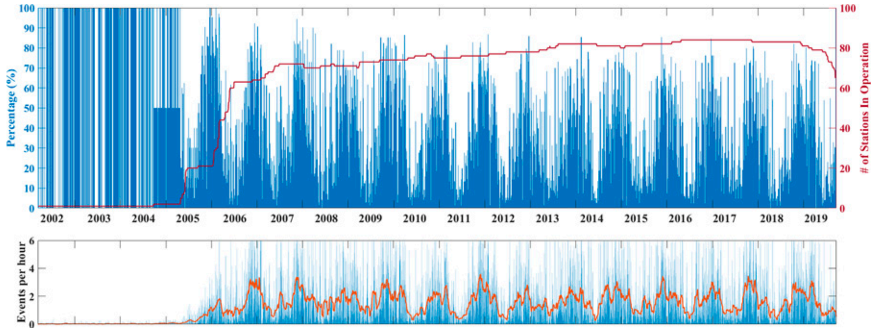

FIG. 4. (top) Daily time series of the fraction of VWSN stations that detected at least one NWE (blue) and the number of stations measuring on a given night (red). The first station started recording data on 11 Mar 2002, and the last day of data used for this study is 19 Sep 2019. (bottom) Daily time series of the hourly frequency of detected NWEs within the VWSN (blue) and the 30-day running mean of the hourly frequency (red).

measure is difficult in this analysis in the absence of an a priori way of determining the propagation direction of individual events. A more detailed analysis of the relationship between synoptic patterns, the occurrence of NWEs, and the relationship between the two phenomena will be the subject of a future study.

Observations show that the duration of intermittent turbulence events (the shortest atmospheric disturbances leading to NWEs) and accompanying NWEs have time scales of about 10–120 min (e.g., Nappo 1991; Sun et al. 2002, 2004, 2015a; Acevedo and Fitzjarrald 2003; White 2009; Deb Burman et al. 2018). The minimal reoccurrence frequency of intermittent turbulence events is on similar time scales (Nappo 1991; Coulter and Doran 2002), consistent with typical observed SBL regime durations (Abraham and Monahan 2019b, 2020; Abraham et al. 2019). Because there is no single event duration or recurrence time scale, we determine ES for a range of $\tau = 1, \ldots, 90$ min.

The Q values can then be used to determine an undirected NWE network across the VWSN stations. A pair of stations will be said to share an NWE link if for all values of τ considered, $Q(\tau) \geq Q_{\text{thresh}}(\tau)$. Otherwise, no NWE link is assigned. In this study, we take the τ-dependent threshold $Q_{\text{thresh}}(\tau)$ to be p95[$Q(\tau)$], the 95th percentile of $Q(\tau)$ values across all pairs of VWSN stations. The resulting network allows analysis of the spatial connectivity structure of NWEs.

4. Results

In this section, we start by summarizing the climatological statistics of observed NWEs. Next, we investigate the distributions of NWEs conditioned on event warming rate quartiles. Last, we characterize the spatial connectivity structure of NWEs across the VWSN.

a. NWE occurrence climatology

The fraction of VWSN stations experiencing NWEs varies substantially from night to night, modulated by a strong seasonal cycle (Fig. 4, upper panel). The number of VWSN stations increased substantially from 2004 to 2006, whereas only a handful of stations were present before this time. From about 2005 onward, the number of reporting VWSN stations (around 80) has been relatively stable. Over this period, the occurrence of NWEs at individual stations show modest interannual variability with occurrence maxima and minima in winter and summer, respectively.

One trivial factor influencing the number of detected NWEs per night is the seasonal variation of nighttime hours. Accounting for this effect by considering the hourly NWE occurrence frequency in the VWSN, a seasonal cycle remains evident (Fig. 4, lower panel). The hourly NWE occurrence frequency across the VWSN (smoothed by a 30-day running mean) changes from larger values of about 3 NWE h^{-1} in the winter to the smallest value of about 1 NWE h^{-1} during the summer.

Within a given night, several NWEs can occur consecutively at a single station (cf. Fig. 1). The pdf of the time between those consecutive NWEs occurrences across all VWSN stations exhibits a clear maximum between approximately 1 and 2 h (Fig. 5). Analyses of consecutive NWEs within a night for individual seasons show similar structures (not shown). This time scale is more likely related to smaller-scale atmospheric disturbances, such as submesoscale phenomena leading to intermittent turbulence events, than to synoptic-scale changes. Strikingly, both the shape and the position of the maximum closely resemble the vSBL event-duration pdfs (time spent within a weakly turbulent state before turbulence recovery) at several stations around the world (cf. Figs. 6 and 5, respectively, in Abraham and Monahan 2019b, 2020). The similarity is intriguing and suggests a possible relationship between the occurrence of NWEs and SBL regime transitions from very to weakly stable conditions. While we do not have stratification information in the VWSN dataset to test this hypothesis, the possibility is an interesting direction of future research.

As is illustrated in Fig. 1, the VWSN dataset shows evidence of different types of NWEs. One characteristic distinguishing NWEs from each other is their event warming rate (EWR), defined as the ratio of the NWE magnitude to the duration of its warming phase:

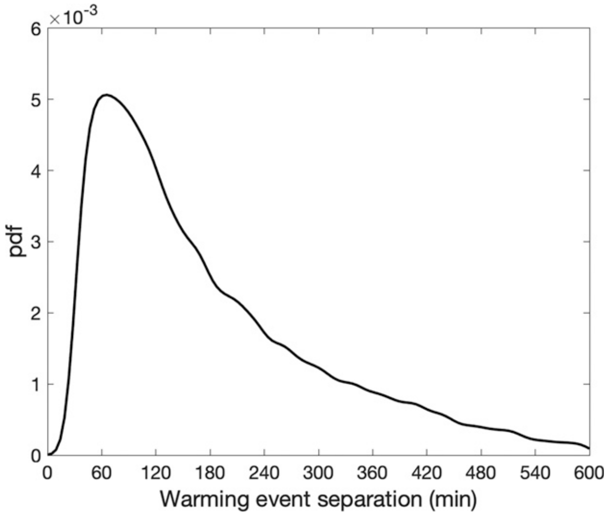

FIG. 5. Probability density function of the time between consecutive NWEs occurring at a given station within the same night, calculated across all VWSN stations.

$$\mathrm{EWR} = \frac{T(t_p) - T(t_s)}{t_p - t_s}. \tag{4}$$

We base a simple classification of NWEs on EWR quartiles, with particular focus on NWEs with the smallest EWRs (Q1-EWR) and largest EWRs (Q4-EWR). This relatively coarse classification is used to balance the competing needs of distinct types of NWEs with retaining a sufficient number of events in each class. The behavior of second and third quartile events is intermediate between Q1-EWR and Q4-EWR events.

Annual cycles of the hourly NWE occurrence frequency in the VWSN are evident for all NWEs as well as for each individual EWR quartile class (Fig. 6). The annual cycle is most pronounced for NWEs in class Q1-EWR and weakest in class Q4-EWR. For all EWR quartile classes, the smallest hourly occurrence frequencies are in May–June and the largest are in November–December.

With the exception of the transitional months of March and October, the monthly EWR-class quartiles show clear differences in hourly occurrence frequencies. From April to September, Q4-EWR is the most common class of NWEs, while NWEs from November to February are dominated by Q1-EWR. This latter finding suggests a relationship between relatively slow-warming phases of Q1-EWR NWEs and large-scale weather changes. In the northern midlatitudes, the occurrence frequency of such large-scale weather changes increases during winter. Short and rapid warmings, such as those occurring in class Q4-EWR, are consistent with the occurrence of intermittent turbulence events. The fact that the annual cycle in occurrence frequency is weakest for Q4-EWR NWEs is consistent with findings that intermittent turbulence events are only weakly related to the synoptic setting and therefore to large-scale weather changes (e.g., Coulter and Doran 2002). The interannual variability of the occurrence frequency of each EWR class is weak (not shown).

b. Distributions of NWE temporal structures

To systematically study the physical properties of different NWEs, we consider temperature time series distributions with a particular focus on NWE-classes Q1-EWR and Q4-EWR, the two end members of the distribution associated with slowest and fastest warming NWEs, respectively. NWEs of the remaining EWR quartiles have intermediate temperature time series such that smooth continuous shifts between EWR-quartile classes occur. To facilitate readability and interpretation of the plots presented we omit EWR-Q2 and EWR-Q3 classes from the discussion. We first consider temperature time series distributions of NWEs at individual stations, then the composite statistical behavior across all VWSN stations.

We also investigated these distributions based on quartiles of other parameters, such as the warming phase duration of the NWEs and their magnitudes. These analyses did not result

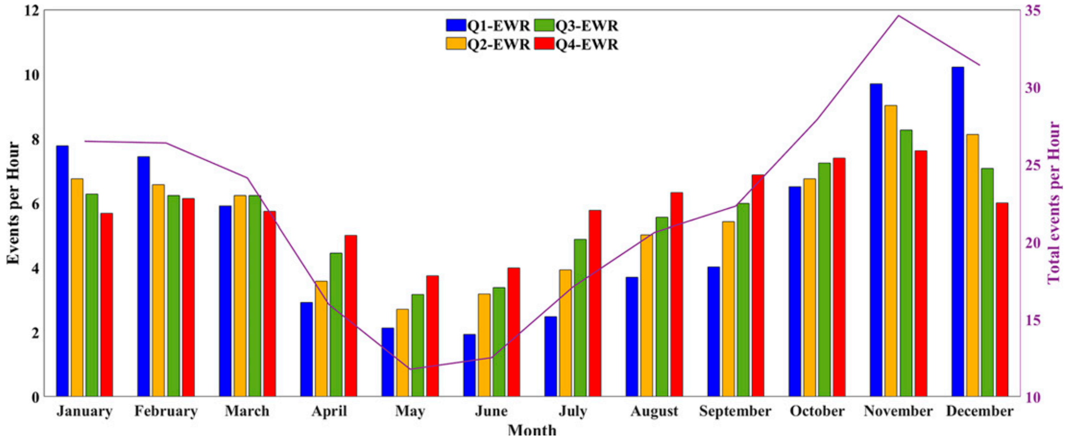

FIG. 6. Annual cycle of detected NWEs per hour within each EWR class from 11 Mar 2002 to 19 Sep 2019. The purple line (scale on the right side) shows the annual cycle of NWE frequency for all events.

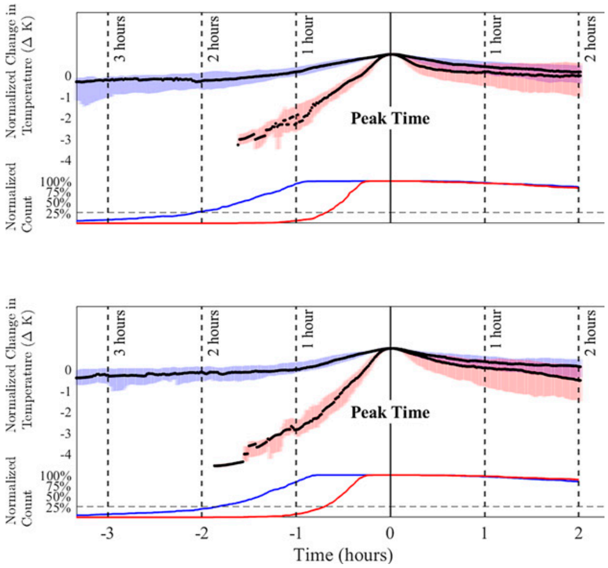

FIG. 7. Distributions of temperature time series of NWEs in class Q1-EWR (blue) and Q4-EWR (red) of the (top) 1281 NWEs identified at the UVic ISC from 11 Mar 2002 to 19 Sep 2019 and (bottom) 1131 NWEs detected at the Sidney station between 28 May 2006 and 19 Sep 2019. NWE time series are centered to have a common time of peak warming and maximum temperature (denoted respectively by 0 h and 0 K). The black line corresponds to the median temperature time series across all NWEs of the particular EWR class, with bars indicating the interquartile range. Normalized count values in the lower part of the panel refers to the number of events used at any given time to compute the temperature distribution in each EWR-quartile, relative to the number at event peak time ($t = 0$ h). The horizontal dashed reference line denotes a normalized count of 20% (that is events above this reference line are shorter).

in as clear a differentiation between events as the EWR, which encompasses both magnitude and duration and provides a clear distinction between different classes of NWEs.

1) INDIVIDUAL STATION COMPOSITES

For each individual station, NWE temperature time series (from t_s to $t_p + 2$ h) are centered at the peak time t_p. The temperature peak $T(t_p)$ is offset so that all NWEs share a common maximum temperature (defined arbitrarily to have the value zero). This standardization of NWEs allows for direct comparison of associated temperature changes across all events at individual stations. Distributions across NWE time series are represented by the median and interquartile range at each time in the event, computed separately for the two quantile classes. The distributions of temperature time series for NWEs of classes Q1-EWR and Q4-EWR at two representative VWSN stations (UVic ISC and Sidney) are shown in the upper panels of Fig. 7. The line plots in the lower panels of Fig. 7 indicate the normalized count of NWEs entering the distributions at each time (relative to 100% at t_p). The normalized counts are the number of events used for the calculations at each time, divided by the number of events at $t = t_p$. Normalized counts of less than 100% for $t < t_p$ result from NWEs having warming phases of differing duration; normalized counts of less than 100% for $t > t_p$ are due to NWEs occurring sufficiently close to sunrise.

By construction, a clear distinction is evident in the distribution of temperature time series distributions preceding t_p, with the interquartile bands of the Q1-EWR and Q4-EWR NWEs well separated. The median temperature time series of the two NWE classes show that NWEs of class Q4-EWR tend to be shorter than and about 3 times as large in magnitude as Q1-EWR events. At both stations, more than 75% of Q4-EWR NWEs have warming phases shorter than an hour (normalized count above the reference line in Fig. 7), while a similar fraction of Q1-EWR NWEs have warming phases of at least 3 h. At neither station does the warming phase of any Q4-EWR NWEs last longer than two hours. Since Q1-EWR and Q4-EWR NWEs are distinguished by the warming rate, not by the magnitude or duration of the warming phase separately, this difference between NWE classes is not simply true by construction.

After the event peak time t_p, a clear distinction between the median temperature time series remains, such that Q1-EWR cool more slowly than Q4-EWR NWEs. The distinction is less pronounced than in the period before t_p, and the interquartile range of Q4-EWR and the median of Q1-EWR NWEs overlap. Nevertheless, this result demonstrates a systematic distinction in temporal structure between NWE classes. In general, NWEs with fast-warming phases cool faster than slowly warming ones. Results similar to those we have presented for the two representative stations are found at all other stations of the VWSN (not shown).

2) COMPOSITES ACROSS STATIONS

Having considered NWE temperature time series distributions at individual stations, we now consider the distribution of composite time series from individual stations across the VWSN. Individual station composites are defined as the median temperature time series within each of the Q1-EWR and Q4-EWR NWE classes (denoted the “station medians”). The distribution of station medians (median and interquartile range) across all stations are illustrated in Fig. 8. The distinction between the typical warming and cooling phases of the temperature distribution time series between Q1-EWR and Q4-EWR NWEs is even clearer across station medians than for temperature time series distributions at individual stations. The station median Q4-EWR NWEs are much larger in magnitude and have much shorter warming phases than Q1-EWR NWEs. Another noteworthy feature of the station median temperature time series is that the post-T-peak cooling for Q4-EWR NWEs is much faster than for Q1-EWR NWEs. In the hour following t_p, station median Q4-EWR NWEs cool particularly rapidly. The relatively narrow interquartile range of the station median temperature time series for both Q1-EWR and Q4-EWR NWEs indicates strong similarity of NWE properties across the whole VWSN domain, despite the differences in local station environment (e.g., urban vs semirural; inland vs coastal).

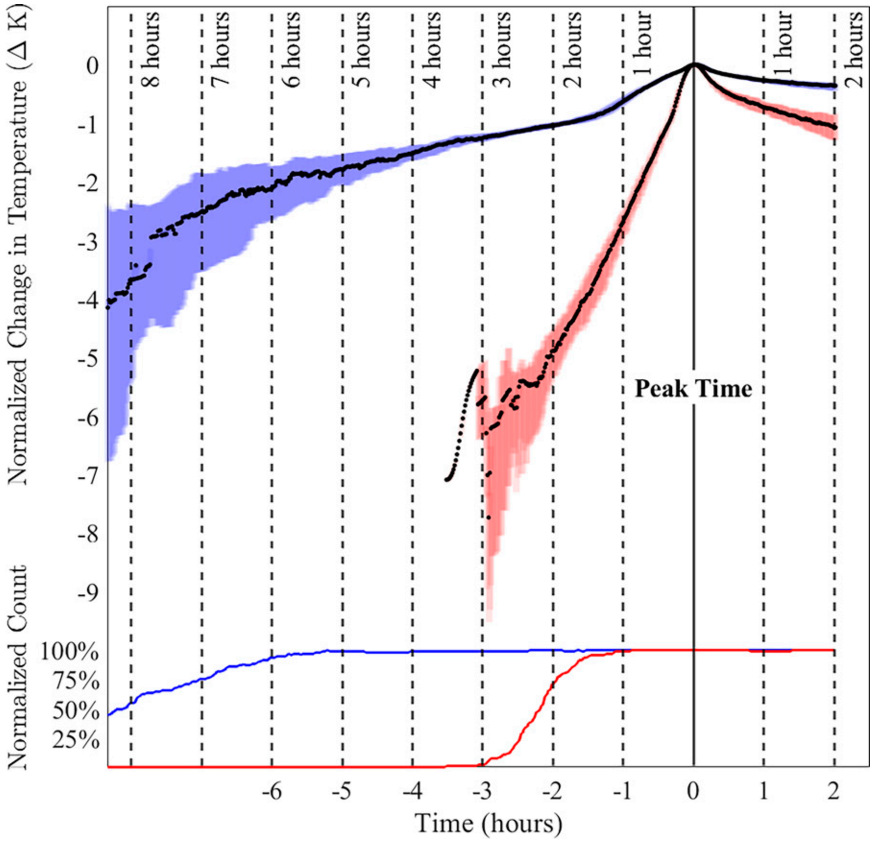

FIG. 8. As in Fig. 7, but for station median temperature time series of NWEs in class Q1-EWR (blue) and Q4-EWR (red) using all VWSN stations. The black lines are the median temperature time series of the particular NWE EWR classes across all VWSN stations, with bars illustrating the respective interquartile ranges. Here, the normalized count refers to number of station medians at each time point entering the estimation of the distribution.

These results demonstrate a robust distinction between rapidly warming and slowly warming NWEs in the VWSN, particularly in terms of the distributions of individual station medians. Consistent with differences in seasonal cycles of event frequency, these differences suggest that the classes of NWEs represent distinct sets of physical processes. Fast surface temperature increases during Q4-EWR NWEs are similar to those during the transition from the vSBL to the wSBL: rapid warming over tens of minutes followed by a return to cooling shortly after t_p (e.g., Fig. 2 in Abraham and Monahan 2019c). Such temperature changes can further be associated with the occurrence of intermittent turbulence bursts. In contrast, slowly warming Q1-EWR NWEs are suggestive of warming associated with frontal changes in cloud cover or horizontal temperature advection. Using ERA5 reanalysis products, we investigated relationships between these two different EWR-classes and the synoptic state (such as large-scale pressure and temperature tendencies; not shown). This analysis did not demonstrate any evident characteristic patterns of the synoptic-scale flow or temperature tendency in association with the occurrence or structure of Q1-EWR and Q4-EWR NWEs. A detailed understanding of the physical mechanisms resulting in the different EWR-classes of NWEs remains unclear.

c. *Spatial structures of NWEs*

1) EVENT SYNCHRONIZATION

To investigate the spatial connectivity of NWEs (across all EWR quartiles), we first analyze the dependence of the pairwise ES measure Q [Eq. (3)] on the distance d between VWSN stations and the time lag τ. The spatial distribution of Q and scatterplots of Q against d for three different representative base stations at $\tau = 60$ min are illustrated in Fig. 9. Evidently, stations in the vicinity of the base stations show larger NWE synchronicity (with Q values between 0.3 and 0.5) than stations farther apart (with Q values below 0.15).

The relationship between d and Q is broadly similar across the three representative VWSN stations. In particular, the overall range of Q values and the rate of decrease with distance are comparable. Some differences in the overall magnitude and spread of Q values are evident for $d < 10$ km. For example, for the UVic ISC station, a

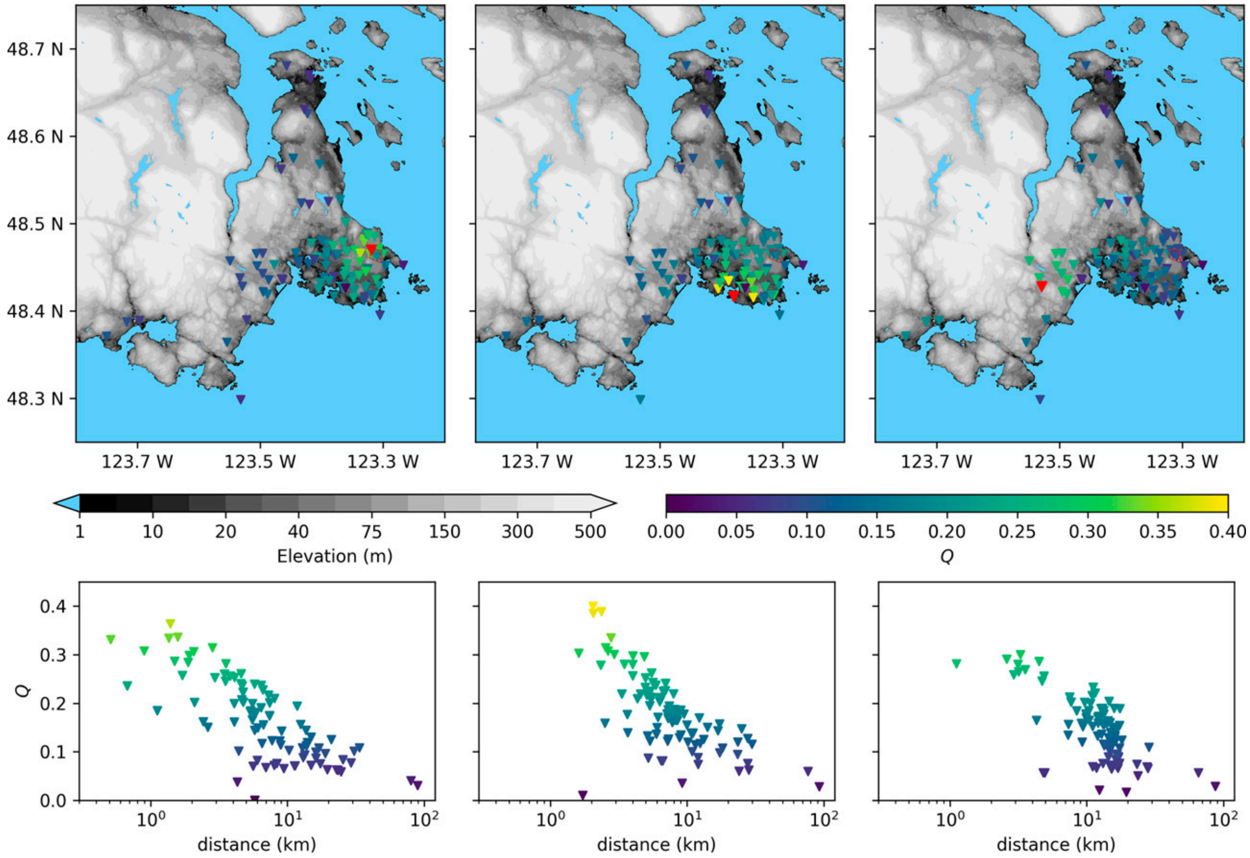

FIG. 9. (top) Pairwise synchronicity values [$Q(\tau = 60$ min)] for three base stations (left) UVic ISC, (center) James Bay, and (right) Happy Valley (cf. Fig. 1). (bottom) Scatterplots show the dependence of Q on the distance of stations relative to the base stations.

relatively large number of other stations are located within a 3-km radius, and Q displays a larger variability (between 0.15 and 0.4) than is found at the other stations (Fig. 9, left panels). This result suggests some influence of the local setting of a station (e.g., topography; proximity to water) on the spatial connectivity of NWEs. We also note that Q values of about 0.2–0.35 are typical for d of about 5 km. This result agrees well with Abraham and Monahan (2020), in which the pairwise occurrence probability of synchronous vSBL-to-wBSL transitions at towers at Los Alamos separated by about 5–8 km (for $\tau = 60$ min) was between 0.3 and 0.45. The slightly elevated probability in Abraham and Monahan (2020) might be related to differences in surface features or in event definition (e.g., while not every NWE necessarily leads to a vSBL to wSBL transition, every vSBL to wSBL transition is accompanied by an NWE). Nonetheless, the similarity in estimated event synchronicity between these two different studies is noteworthy.

Considering pairwise Q values for all τ (Fig. 10) several relationships are evident:

1) The Q increases rapidly with τ up to $30 < \tau < 45$ min, after which the dependence becomes weaker, that is, the slope of $Q(\tau)$ changes considerably in that τ range (Figs. 10a–d). Increasing τ allows Q to capture more events with finite propagation speed, but also increases the probability of capturing unrelated events that are synchronous by chance within the time window. Beyond a value of $\tau \sim 45$ min, Q is only weakly sensitive to τ, suggesting that this window is sufficiently large to capture most of the true propagating synchronous events. Further evidence for this interpretation is that the saturation values of Q are reached at smaller τ for closer station pairs.
2) The Q values are more variable across station pairs for smaller values of d (Figs. 10c–d). This demonstrates the influence of local features on the spatial connectivity of NWEs. Although the mechanisms generating the warming events may be of relatively large scale, local surface heterogeneity can influence local responses and reduce values of Q for smaller values of d.
3) For a given τ, the relationship between d and Q follows approximately a power-law relationship (Figs. 10e–j; red lines are least squares fits).
4) Decreasing τ results in increasing frequency of no event synchronicity ($Q = 0$) between stations more than 1 km apart, with little effect for stations closer than about 1 km (Figs. 10k–p).

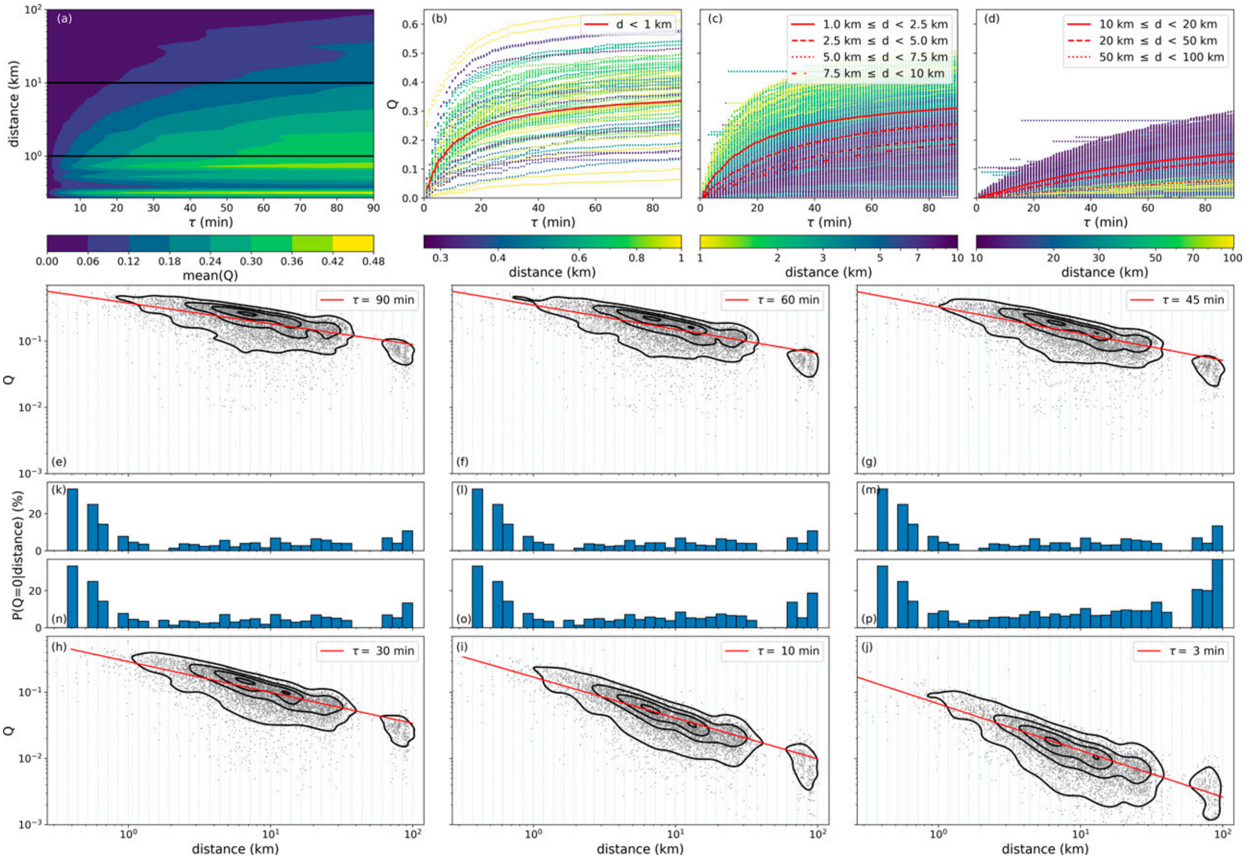

FIG. 10. (a) Mean pairwise synchronicity values Q as a function of time lag τ and interstation distance d, and Q as a function of τ for all station pairs with d (b) less than 1 km, (c) between 1 and 10 km, and (d) more than 10 km apart. Different means are illustrated in red. Also shown are scatterplots of Q against d for 6 different τ: (e) 90, (f) 60, (g) 45, (h) 30, (i) 10, and (j) 3 min. Bivariate probability density estimates are illustrated with black contour lines, and linear regression lines are shown in red. Last, bar plots display the fraction of data $Q = 0$ [for the six different τ: (k) 90, (l) 60, (m) 45, (n) 30, (o) 10, and (p) 3 min] binned by interstation distances. Bivariate probability density estimates are calculated with the multivariate kernel density estimation of O'Brien et al. (2014, 2016).

This analysis is repeated for NWEs in classes Q1-EWR (slow warming) and Q4-EWR (fast warming) separately. NWEs in class Q1-EWR show qualitatively similar characteristics to those for all classes taken together (not shown). In contrast, for NWEs of class Q4-EWR, the characteristics of the relationships between Q, τ, and d are substantially different. For these fast-warming NWEs, Q values are independent of τ for station pairs with $d < 10$ km (Figs. 11a–d). In other words, NWEs of class Q4-EWR occur either simultaneously across domains with breadths of about 10 km or occur only at a single station. Stations farther apart ($d > 10$ km) exhibit an increase in Q values with increasing τ up to their Q-saturation value. However, the majority of station pairs still exhibit no dependence of Q values on τ. In fact, for Q4-EWR events $Q = 0$ for most station pairs independent of d or τ (Figs. 11h–j). These results indicate that NWEs of class Q4-EWR are much more temporally localized than other NWEs, consistent with the interpretation that such NWEs are associated with intermittent turbulence bursts. Likely because synchronous occurrences of NWEs in class Q4-EWR are rare, no clear power-law relationship between Q and d is evident (Figs. 11e–g). In general, Q decreases with increasing d, but the scatter around the regression line is considerable.

There is no evident seasonal variation in the relationship between Q, d, and τ (not shown).

2) NETWORK ANALYSIS

As described in section 3, station pair Q values are used to construct an undirected network to represent the spatial connectivity of NWEs in the greater Victoria region. In our analysis, we connect two VWSN stations with a link if for all $1 \le \tau \le 90$ min, the $Q(\tau)$ values between those VWSN stations are above the 95th percentile, p95[$Q(\tau)$,] of all pairwise $Q(\tau)$ values in the VWSN. The dependence of p95[$Q(\tau)$] on τ as well as the resulting NWE connectivity network is illustrated in Fig. 12.

The dependence of p95(Q) on τ demonstrates the familiar behavior of largest increases for small τ and a subsequent flattening toward a Q-saturation limit (Fig. 12a). Since p95(Q) is calculated over the entire range of d values, the Q-saturation

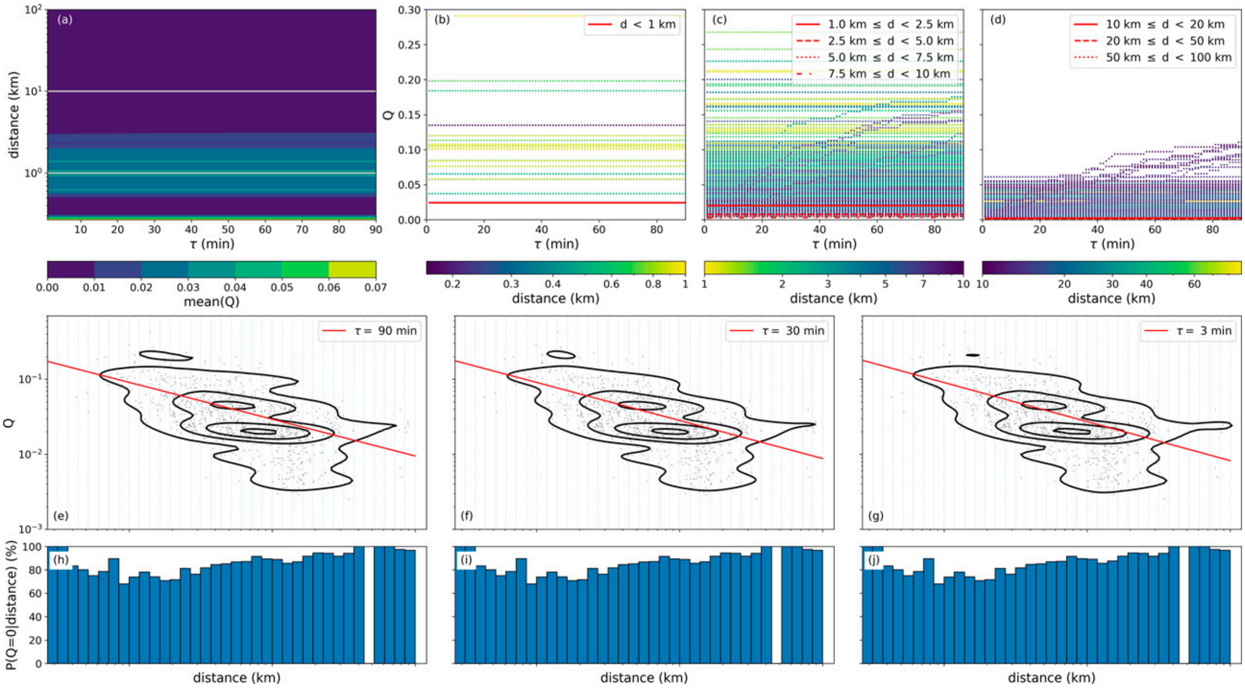

FIG. 11. As in Fig. 10, but for NWEs of class Q4-EWR.

value is not reached within the range of τ values examined here. The spatial connectivity structures of NWEs exhibit a relatively unorganized NWE connectivity network; neither dominant connectivity directions, nor clear relationships to the local topography are obvious (Fig. 12c).

The VWSN link probability (the ratio of links of length d to the number of station pairs of that distance; Fig. 12b) is weakly sensitive to d for $d \simeq 1$ km and decreases with d for larger station separations. Network links are only found for stations less than 4 km apart. In principle, the link probability should approach 1 as $d \rightarrow 0$. Again, the relatively small Q values for station pairs with $d < 1$ km suggests that small-scale surface heterogeneities have a substantial effect on the spatial structures of NWEs, especially with regard to localized NWEs such as those associated with class Q4-EWR.

We analyze whether preferred VWSN connectivity directions exist by examining the relationship between the geographic orientation of links and the link strength for $Q(\tau = 60 \text{ min})$. The analysis is then compared with the relationship between link orientation and link strength in 10 randomly constructed networks that are determined using the same VWSN stations and the NWE link probability (Fig. 12b). For each random network, Q values are assigned to links using the power-law relationship between d and Q and the $Q(d) = 0$ probability for $\tau = 60$ min. By construction, the random networks do not show any preferred relationship between Q and direction; the same is observed in the true NWE network within the VWSN (Fig. 13).

The network analysis based on Q1-EWR NWEs alone resembles structures and link probabilities of the analysis over all NWE classes (not shown). Both networks (using all and slow-warming NWEs) show no evidence of preferred link centers. In contrast, the network associated with Q4-EWR events alone is dominated by a small number of centers (Fig. 14a). These centers are typically at higher elevation, although not all high-elevation stations are link centers. The VWSN link probabilities for Q4-EWR NWEs are well approximated by an exponential dependence on station separation, $\exp(-d/\delta)$, with $\delta \sim 0.6$ km (Fig. 14b). In contrast to the link probability using all NWEs over all EWR classes, this relatively simple functional relationship for Q4-EWR NWEs holds across all d. As with the network analysis for all NWEs, the network for NWEs of class Q4-EWR does not exhibit preferred link directions (Fig. 14c).

Seasonal network analysis also shows generally unstructured networks without any particular geographic connectivity directions or relationship to the local topography (not shown).

5. Conclusions and future work

Using temperature measurements from the Vancouver Island School-Based Weather Station Network in British Columbia, we have determined the temporal and spatial characteristics of nocturnal warming events. The climatological occurrence frequency of NWEs has a clear seasonal cycle, with a larger hourly rate of NWE detection in winter months and a lower rate in summer months. Temperature time series of NWEs conditioned on warming rate quartiles show markedly different temporal characteristics. Slow-

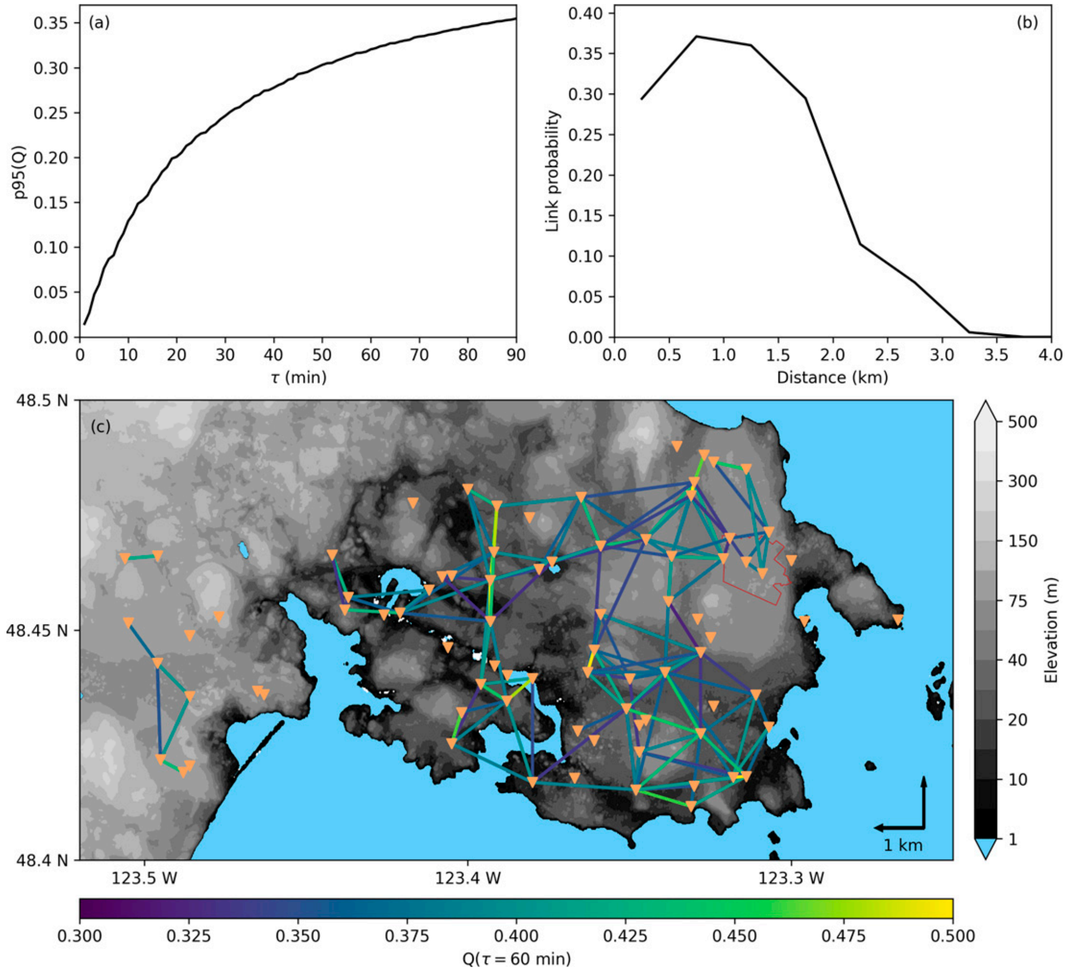

FIG. 12. (a) The 95th-percentile Q as a function of τ. (b) Network link probability for NWEs as a function of interstation distance (black). (c) Network of NWE in the VWSN. A link between two stations is determined when all Q values for $\tau = 1, \ldots, 90$ min are above their respective 95th percentile [in (a)]. Link colors illustrate $Q(\tau = 60 \text{ min})$. The topographic data are as in Fig. 1.

warming NWEs have low amplitudes, while fast-warming NWEs show temperature increases of several kelvins. Conditioning temperature time series on the warming rates also results in distinct temporal behavior of temperature time series after events reach their peak temperatures; fast-warming NWEs cool rapidly and have narrow temperature peaks, while slow-warming NWEs also cool slowly. The median behavior of the NWE classes at individual stations is similar across all VWSN stations.

Spatial characteristics of NWEs are determined using an event synchronicity metric Q in which two NWEs at different stations separated by the distance d are taken to be related to the same atmospheric disturbance if they occur within a certain time window τ. Values of Q based on all NWE events typically saturate for time scales greater than an hour. Smaller distances d generally show larger variability in Q, suggesting that surface heterogeneities affect the spatial synchronization of NWEs. The synchronicity of fast-warming NWEs depends only weakly on τ, indicating that those NWEs occur either simultaneously across a number of stations or are localized at a single station.

The pairwise Q values are used to construct undirected networks to study the spatial connectivity structures of NWEs. We find that the resulting network is largely unstructured, that is, there is no evidence of NWE spatial connectivity structures that are clearly related to the local topography or preferred orientations. Since VWSN stations are distributed in accordance with the local infrastructure (hence are not randomly distributed in space) we compare the observed network with randomly constructed networks using observed link probabilities and pairwise Q values dependent on interstation distances. The fact that the actual network and randomly constructed networks share the similar characteristics supports the conclusion that the observed network is truly unstructured. Even though the number of detected NWEs changes with the season, the determined event synchronicity values, as well as

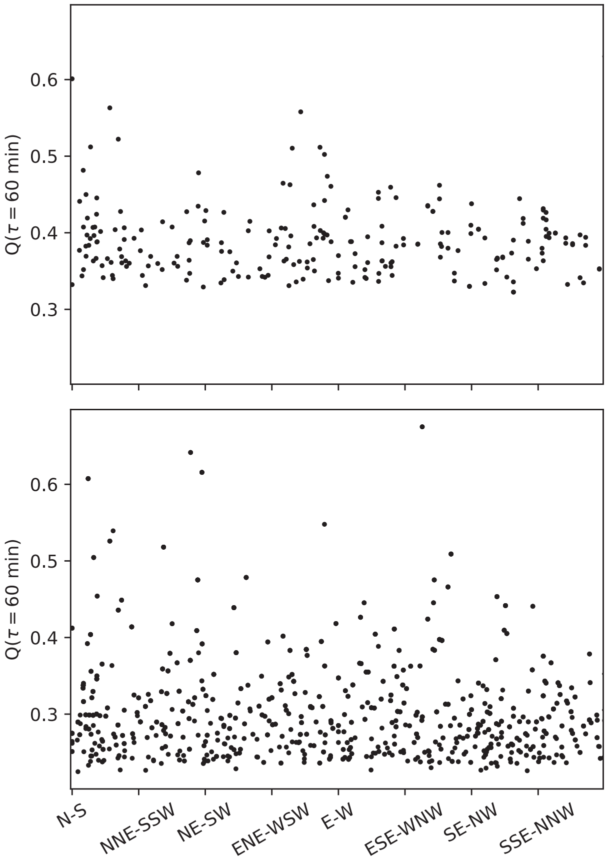

FIG. 13. (top) Scatterplot of orientations of network links against their corresponding synchronicity measure Q. (bottom) As in the top panel, but for 10 random networks using the same stations as the VWSN and observed network link probabilities (Fig. 12b), power-law relationship between interstation distance and Q values (Fig. 10f), and the $Q(d) = 0$ probability for $\tau = 60$ min (Fig. 10l).

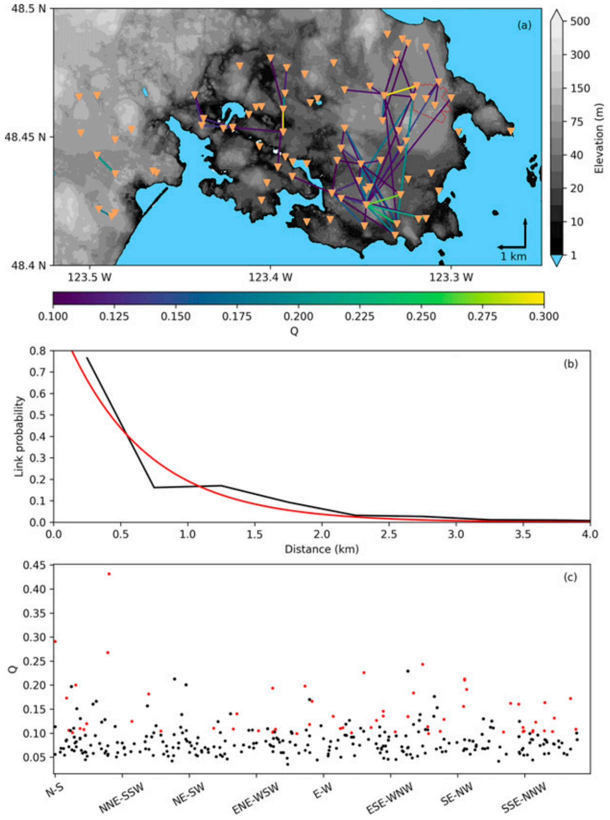

FIG. 14. (a) As in Fig. 12c, but for NWEs of class Q4-EWR and using the 95th percentile for $Q(\tau = 10$ min) as the network link criterion. (b) Network link probability for NWEs of class Q4-EWR as a function of interstation distance (black) compared with a least squares exponential fit (red). (c) Scatterplot of orientations of network links for NWEs of class Q4-EWR against their corresponding synchronicity measure Q (red). Black dots illustrate the same measure for 10 random networks generated as in Fig. 13, using values from Fig. 11.

related network structures are largely unchanged over the course of the year.

One possible reason for the lack of structure in the empirical networks is that the identified NWEs are related to different atmospheric processes with widely different temporal and spatial scales. For instance, while slowly warming NWEs may be associated with large-scale synoptic changes, fast-warming NWEs could be associated with small-scale intermittent turbulence events. In support of this interpretation, the network constructed from the quartile of fastest warming NWEs (which seems to include many intermittent turbulence events) is more localized than that constructed from all NWEs. However, the observations available for the present analysis do not allow for an unambiguous characterization of the different causes of the NWEs.

The results demonstrate that the spatial coherence of NWEs is weak on scales of more than a few kilometers, which is at or below the resolution of most weather and climate models. For example, our results provide guidance on how such NWE processes should be parameterized, that is, whether deterministic or stochastic parameterizations are applicable (Bessac et al. 2019; Abraham et al. 2019). Deterministic parameterizations are appropriate when a scale separation exists between the parameterized subgrid-scale processes and the resolved scales; otherwise, the subgrid-scale tendencies are not expected to depend deterministically on the resolved state.

In a future study we will conduct a more detailed network analysis in which identified NWEs are first conditioned on distinct prevailing large-scale synoptic flow patterns over the greater Victoria region. This approach will allow determining which types of NWEs (i.e., which typical temporal structures) are particular to a large-scale flow pattern and whether more structured networks and clearer propagation patterns of NWEs can be found. For that analysis we will also compare the undirected network criteria used in this study with directed network criteria (e.g., Rheinwalt et al. 2012, 2016). Another approach to investigate propagation patterns of NWEs includes network trajectory analyses in which typical trajectories through the VWSN are mapped. Such analyses may reveal a clearer influence of the local topography. Furthermore, they would allow the study of temporal propagation patterns of different classes of NWEs within the VWSN. Typical NWE propagation patterns and structures could also be compared with large-eddy simulations in idealized topographical settings (with different typical large-scale forcing) to understand the influence of complex terrain on these spatially variable nighttime disturbances.

A more detailed study on the fast-warming NWEs is required, as such events appear to hold information about the spatial structure of intermittent turbulence events. As intermittent turbulence events are one of the causes of turbulence regime transitions within the stable boundary layer, understanding their spatial structure is important for improving simulations of the nocturnal boundary layer in models for weather and climate (e.g., Abraham et al. 2019). For example, wavelet analysis can be used to extract temperature time series characteristic of intermittent turbulence events. Even though it contains only surface information, the high-resolution and long-term VWSN in the greater Victoria region is a unique dataset allowing investigation of a range of boundary layer processes that is much broader than was considered in this analysis.

Acknowledgments. The VWSN is maintained by a partnership of the University of Victoria and 12 British Columbia school districts: 61 (Victoria), 62 (Sooke), 63 (Saanich), 64 (Gulf Islands), 68 (Nanaimo), 69 (Qualicum), 70 (Alberni), 71 (Comox Valley), 72 (Campbell River), 79 (Cowichan Valley), 84 (Vancouver Island West), and 85 (Vancouver Island North). The VWSN has received funding from the BC Year of Science, the Natural Sciences and Engineering Research Council (NSERC) PromoScience Program, NEC Corporation, CTV Vancouver Island, the Faculty of Science at the University of Victoria, and generous donations from a number of individuals. Furthermore, the VWSN has received in-kind contributions from Davis Instruments Corporation. The VWSN was founded by Andrew Weaver; we greatly appreciate his hard work in supporting the network for many years. Authors Lao and Monahan acknowledge support of NSERC RGPIN-2019-04986. We also thank three anonymous reviewers for helpful comments that improved our paper.

Data availability statement. All observations from the VWSN are stored and published on the VWSN website (https://victoriaweather.ca/). For more information contact weather@uvic.ca. The Japan Aerospace Exploration Agency (JAXA) is thanked for providing data of topographical elevation from the Advanced Land Observing Satellite (ALOS) Global Digital Surface Model (https://global.jaxa.jp/projects/sat/alos/). Hourly observations from the Environment and Climate Change Canada weather station at the University of Victoria can be obtained online (https://climate.weather.gc.ca/historical_data/search_historic_data_e.html).

REFERENCES

Abraham, C., and A. H. Monahan, 2019a: Climatological features of the weakly and very stably stratified nocturnal boundary layers. Part I: State variables containing information about regime occupation. *J. Atmos. Sci.*, **76**, 3455–3484, https://doi.org/10.1175/JAS-D-18-0261.1.

——, and ——, 2019b: Climatological features of the weakly and very stably stratified nocturnal boundary layers. Part II: Regime occupation and transition statistics and the influence of external drivers. *J. Atmos. Sci.*, **76**, 3485–3504, https://doi.org/10.1175/JAS-D-19-0078.1.

——, and ——, 2019c: Climatological features of the weakly and very stably stratified nocturnal boundary layers. Part III: The structure of meteorological state variables in persistent regime nights and across regime transitions. *J. Atmos. Sci.*, **76**, 3505–3527, https://doi.org/10.1175/JAS-D-18-0274.1.

——, and ——, 2020: Spatial dependence of stably stratified nocturnal boundary-layer regimes in complex terrain. *Bound.-Layer Meteor.*, **177**, 19–47, https://doi.org/10.1007/s10546-020-00532-xx.

——, A. M. Holdsworth, and A. H. Monahan, 2019: A prototype stochastic parameterization of regime behaviour in the stably stratified atmospheric boundary layer. *Nonlinear Processes Geophys.*, **26**, 401–427, https://doi.org/10.5194/npg-26-401-2019.

Acevedo, O. C., and D. R. Fitzjarrald, 2001: The early evening surface-layer transition: Temporal and spatial variability. *J. Atmos. Sci.*, **58**, 2650–2667, https://doi.org/10.1175/1520-0469(2001)058<2650:TEESLT>2.0.CO;2.

——, and ——, 2003: In the core of the night-effects of intermittent mixing on a horizontally heterogeneous surface. *Bound.-Layer Meteor.*, **106**, 1–33, https://doi.org/10.1023/A:1020824109575.

——, F. D. Costa, P. E. S. Oliveira, F. S. Puhales, G. A. Degrazia, and D. R. Roberti, 2014: The influence of submeso processes on stable boundary layer similarity relationships. *J. Atmos. Sci.*, **71**, 207–225, https://doi.org/10.1175/JAS-D-13-0131.1.

——, L. Mahrt, F. S. Puhales, F. D. Costa, L. E. Medeiros, and G. A. Degrazia, 2016: Contrasting structures between the decoupled and coupled states of the stable boundary layer. *Quart. J. Roy. Meteor. Soc.*, **142**, 693–702, https://doi.org/10.1002/qj.2693.

——, R. Maroneze, F. D. Costa, F. S. Puhales, L. G. Nogueira Martins, P. E. Soares de Oliveira, and L. Mortarini, 2019: The nocturnal boundary layer transition from weakly to very stable. Part 1: Observations. *Quart. J. Roy. Meteor. Soc.*, **145**, 3577–3592, https://doi.org/10.1002/qj.3642.

Agarwal, A., N. Marwan, M. Rathinasamy, B. Merz, and J. Kurths, 2017: Multi-scale event synchronization analysis for unravelling climate processes: A wavelet-based approach. *Nonlinear Processes Geophys.*, **24**, 599–611, https://doi.org/10.5194/npg-24-599-2017.

Bessac, J., A. H. Monahan, H. M. Christensen, and N. Weitzel, 2019: Stochastic parameterization of subgrid-scale velocity enhancement of sea surface fluxes. *Mon. Wea. Rev.*, **147**, 1447–1469, https://doi.org/10.1175/MWR-D-18-0384.1.

Blay-Carreras, E., and Coauthors, 2014: Role of the residual layer and large-scale subsidence on the development and evolution of the convective boundary layer. *Atmos. Chem. Phys.*, **14**, 4515–4530, https://doi.org/10.5194/acp-14-4515-2014.

Boers, N., B. Bookhagen, N. Marwan, J. Kurths, and J. Marengo, 2013: Complex networks identify spatial patterns of extreme rainfall events of the South American Monsoon System. *Geophys. Res. Lett.*, **40**, 4386–4392, https://doi.org/10.1002/grl.50681.

Bonin, T. A., W. G. Blumberg, P. M. Klein, and P. B. Chilson, 2015: Thermodynamic and turbulence characteristics of the southern Great Plains nocturnal boundary layer under differing turbulent regimes. *Bound.-Layer Meteor.*, **157**, 401–420, https://doi.org/10.1007/s10546-015-0072-2.

Boyko, V., and N. Vercauteren, 2021: Multiscale shear forcing of turbulence in the nocturnal boundary layer: A statistical analysis. *Bound.-Layer Meteor.*, **179**, 43–72, https://doi.org/10.1007/s10546-020-00583-0.

Cava, D., L. Mortarini, U. Giostra, R. Richiardone, and D. Anfossi, 2017: A wavelet analysis of low-wind-speed submeso motions in a nocturnal boundary layer. *Quart. J. Roy. Meteor. Soc.*, **143**, 661–669, https://doi.org/10.1002/qj.2954.

——, ——, ——, O. Acevedo, and G. Katul, 2019: Submeso motions and intermittent turbulence across a nocturnal low-level jet: A self-organized criticality analogy. *Bound.-Layer Meteor.*, **172**, 17–43, https://doi.org/10.1007/s10546-019-00441-8.

Cheung, K. K. W., and U. Ozturk, 2020: Synchronization of extreme rainfall during the Australian summer monsoon: Complex network perspectives. *Chaos*, **30**, 063117, https://doi.org/10.1063/1.5144150.

Conticello, F., F. Cioffi, B. Merz, and U. Lall, 2018: An event synchronization method to link heavy rainfall events and large-scale atmospheric circulation features. *Int. J. Climatol.*, **38**, 1421–1437, https://doi.org/10.1002/joc.5255.

Conticello, F. R., F. Cioffi, U. Lall, and B. Merz, 2020: Synchronization and delay between circulation patterns and high streamflow events in Germany. *Water Resour. Res.*, **56**, e2019WR025598, https://doi.org/10.1029/2019WR025598.

Coulter, R. L., and J. C. Doran, 2002: Spatial and temporal occurrences of intermittent turbulence during CASES-99. *Bound.-Layer Meteor.*, **105**, 329–349, https://doi.org/10.1023/A:1019993703820.

Deb Burman, P. K., T. V. Prabha, R. Morrison, and A. Karipot, 2018: A case study of turbulence in the nocturnal boundary layer during the Indian summer monsoon. *Bound.-Layer Meteor.*, **169**, 115–138, https://doi.org/10.1007/s10546-018-0364-4.

Edwards, J. M., 2009a: Radiative processes in the stable boundary layer: Part I. Radiative aspects. *Bound.-Layer Meteor.*, **131**, 105, https://doi.org/10.1007/s10546-009-9364-8.

——, 2009b: Radiative processes in the stable boundary layer: Part II. The development of the nocturnal boundary layer. *Bound.-Layer Meteor.*, **131**, 127–146, https://doi.org/10.1007/s10546-009-9363-9.

Evins, R., R. Alexandra, E. Wiebe, M. Wood, and M. Eames, 2020: The impact of local variations in a temperate maritime climate on building energy use. *J. Build. Perform. Simul.*, **13**, 167–181, https://doi.org/10.1080/19401493.2018.1536167.

Ha, K.-J., and L. Mahrt, 2003: Radiative and turbulent fluxes in the nocturnal boundary layer. *Tellus*, **55A**, 317–327, https://doi.org/10.3402/tellusa.v55i4.12103.

Holtslag, A. A. M., and Coauthors, 2013: Stable atmospheric boundary layers and diurnal cycles: Challenges for weather and climate models. *Bull. Amer. Meteor. Soc.*, **94**, 1691–1706, https://doi.org/10.1175/BAMS-D-11-00187.1.

Hoover, J. D., D. R. Stauffer, S. J. Richardson, L. Mahrt, B. J. Gaudet, and A. Suarez, 2015: Submeso motions within the stable boundary layer and their relationships to local indicators and synoptic regime in moderately complex terrain. *J. Appl. Meteor. Climatol.*, **54**, 352–369, https://doi.org/10.1175/JAMC-D-14-0128.1.

Hu, X.-M., P. M. Klein, M. Xue, A. Shapiro, and A. Nallapareddy, 2013: Enhanced vertical mixing associated with a nocturnal cold front passage and its impact on near-surface temperature and ozone concentration. *J. Geophys. Res. Atmos.*, **118**, 2714–2728, https://doi.org/10.1002/jgrd.50309.

Kang, Y., D. Belušić, and K. Smith-Miles, 2015: Classes of structures in the stable atmospheric boundary layer. *Quart. J. Roy. Meteor. Soc.*, **141**, 2057–2069, https://doi.org/10.1002/qj.2501.

Lapo, K., A. Freundorfer, A. Fritz, J. Schneider, J. Olesch, W. Babel, and C. K. Thomas, 2021: The Large-Eddy Observatory Voitsumra Experiment 2019 (LOVE19) with high-resolution, spatially-distributed observations of air temperature, wind speed, and wind direction from fiber-optic distributed sensing, towers, and ground-based remote sensing. *Earth Syst. Sci. Data*, **14**, 885–906, https://doi.org/10.5194/essd-14-885-2022.

Ma, Y., Y. Yang, X.-M. Hu, and R. Gan, 2015: Characteristics and mechanisms of the sudden warming events in the nocturnal atmospheric boundary layer: A case study using WRF. *J. Meteor. Res.*, **29**, 747–763, https://doi.org/10.1007/s13351-015-4101-3.

Mahrt, L., 1998: Nocturnal boundary-layer regimes. *Bound.-Layer Meteor.*, **88**, 255–278, https://doi.org/10.1023/A:1001171313493.

——, 2010: Common microfronts and other solitary events in the nocturnal boundary layer. *Quart. J. Roy. Meteor. Soc.*, **136**, 1712–1722, https://doi.org/10.1002/qj.694.

——, 2014: Stably stratified atmospheric boundary layers. *Annu. Rev. Fluid Mech.*, **46**, 23–45, https://doi.org/10.1146/annurev-fluid-010313-141354.

——, 2017: Heat flux in the strong-wind nocturnal boundary layer. *Bound.-Layer Meteor.*, **163**, 161–177, https://doi.org/10.1007/s10546-016-0219-9.

——, 2019: Microfronts in the nocturnal boundary layer. *Quart. J. Roy. Meteor. Soc.*, **145**, 546–562, https://doi.org/10.1002/qj.3451.

——, C. K. Thomas, and J. H. Prueger, 2009: Space–time structure of mesoscale motions in the stable boundary layer. *Quart. J. Roy. Meteor. Soc.*, **135**, 67–75, https://doi.org/10.1002/qj.348.

——, ——, S. Richardson, N. Seaman, D. Stauffer, and M. Zeeman, 2013: Non-stationary generation of weak turbulence for very stable and weak-wind conditions. *Bound.-Layer Meteor.*, **147**, 179–199, https://doi.org/10.1007/s10546-012-9782-x.

——, J. Sun, and D. Stauffer, 2015: Dependence of turbulent velocities on wind speed and stratification. *Bound.-Layer Meteor.*, **155**, 55–71, https://doi.org/10.1007/s10546-014-9992-5.

——, L. Pfister, and C. K. Thomas, 2020: Small-scale variability in the nocturnal boundary layer. *Bound.-Layer Meteor.*, **174**, 81–98, https://doi.org/10.1007/s10546-019-00476-x.

——, D. Belušič, and O. Acevedo, 2021: Small-scale spatial variation of the nocturnal wind field. *Bound.-Layer Meteor.*, **180**, 225–245, https://doi.org/10.1007/s10546-021-00627-z.

Malik, N., N. Marwan, and J. Kurths, 2010: Spatial structures and directionalities in monsoonal precipitation over South Asia. *Nonlinear Processes Geophys.*, **17**, 371–381, https://doi.org/10.5194/npg-17-371-2010.

——, B. Bookhagen, N. Marwan, and J. Kurths, 2012: Analysis of spatial and temporal extreme monsoonal rainfall over South Asia using complex networks. *Climate Dyn.*, **39**, 971–987, https://doi.org/10.1007/s00382-011-1156-4.

Maroneze, R., O. C. Acevedo, F. S. Puhales, G. Demarco, and L. Mortarini, 2019: The nocturnal boundary layer transition from weakly to very stable. Part II: Numerical simulation with a second order model. *Quart. J. Roy. Meteor. Soc.*, **145**, 3593–3608, https://doi.org/10.1002/qj.3643.

——, ——, F. D. Costa, F. S. Puhales, V. Anabor, D. N. Lemes, and L. Mortarini, 2021: How is the two-regime stable boundary layer reproduced by the different turbulence parametrizations in the weather research and forecasting model? *Bound.-Layer Meteor.*, **178**, 383–413, https://doi.org/10.1007/s10546-020-00581-2.

Medeiros, L. E., and D. R. Fitzjarrald, 2014: Stable boundary layer in complex terrain. Part I: Linking fluxes and intermittency to an average stability index. *J. Appl. Meteor. Climatol.*, **53**, 2196–2215, https://doi.org/10.1175/JAMC-D-13-0345.1.

——, and ——, 2015: Stable boundary layer in complex terrain. Part II: Geometrical and sheltering effects on mixing. *J. Appl. Meteor. Climatol.*, **54**, 170–188, https://doi.org/10.1175/JAMC-D-13-0346.1.

Monahan, A. H., T. Rees, Y. He, and N. McFarlane, 2015: Multiple regimes of wind, stratification, and turbulence in the stable boundary layer. *J. Atmos. Sci.*, **72**, 3178–3198, https://doi.org/10.1175/JAS-D-14-0311.1.

Mortarini, L., S. Maldaner, L. P. Moor, M. B. Stefanello, O. Acevedo, G. Degrazia, and D. Anfossi, 2016: Temperature autocorrelation and spectra functions in low-wind meandering conditions. *Quart. J. Roy. Meteor. Soc.*, **142**, 1881–1889, https://doi.org/10.1002/qj.2796.

——, D. Cava, U. Giostra, F. D. Costa, G. Degrazia, D. Anfossi, and O. Acevedo, 2019: Horizontal meandering as a distinctive feature of the stable boundary layer. *J. Atmos. Sci.*, **76**, 3029–3046, https://doi.org/10.1175/JAS-D-18-0280.1.

Nallapareddy, A., A. Shapiro, and J. J. Gourley, 2011: A climatology of nocturnal warming events associated with cold-frontal passages in Oklahoma. *J. Appl. Meteor. Climatol.*, **50**, 2042–2061, https://doi.org/10.1175/JAMC-D-11-020.1.

Nappo, C. J., 1991: Sporadic breakdowns of stability in the PBL over simple and complex terrain. *Bound.-Layer Meteor.*, **54**, 69–87, https://doi.org/10.1007/BF00119413.

O'Brien, T. A., W. D. Collins, S. A. Rauscher, and T. D. Ringler, 2014: Reducing the computational cost of the ECF using a nuFFT: A fast and objective probability density estimation method. *Comput. Stat. Data Anal.*, **79**, 222–234, https://doi.org/10.1016/j.csda.2014.06.002.

——, K. Kashinath, N. R. Cavanaugh, W. D. Collins, and J. P. O'Brien, 2016: A fast and objective multidimensional kernel density estimation method: fastKDE. *Comput. Stat. Data Anal.*, **101**, 148–160, https://doi.org/10.1016/j.csda.2016.02.014.

Petenko, I., S. Argentini, G. Casasanta, C. Genthon, and M. Kallistratova, 2019: Stable surface-based turbulent layer during the polar winter at Dome C, Antarctica: Sodar and in situ observations. *Bound.-Layer Meteor.*, **171**, 101–128, https://doi.org/10.1007/s10546-018-0419-6.

Pfister, L., K. Lapo, L. Mahrt, and C. K. Thomas, 2021a: Thermal submeso motions in the nocturnal stable boundary layer. Part 2: Generating mechanisms and implications. *Bound.-Layer Meteor.*, **180**, 203–224, https://doi.org/10.1007/s10546-021-00619-z.

——, ——, ——, and ——, 2021b: Thermal submesoscale motions in the nocturnal stable boundary layer. Part 1: Detection and mean statistics. *Bound.-Layer Meteor.*, **180**, 187–202, https://doi.org/10.1007/s10546-021-00618-0.

Quian Quiroga, R., T. Kreuz, and P. Grassberger, 2002: Event synchronization: A simple and fast method to measure synchronicity and time delay patterns. *Phys. Rev.*, **66E**, 041904, https://doi.org/10.1103/PhysRevE.66.041904.

Rabinovich, A. B., J. Šepić, and R. E. Thomson, 2020: The meteorological tsunami of 1 November 2010 in the southern Strait of Georgia: A case study. *Nat. Hazards*, **106**, 1503–1544, https://doi.org/10.1007/s11069-020-04203-5.

Reina, N., and L. Mahrt, 2005: A study of intermittent turbulence with CASES-99 tower measurements. *Bound.-Layer Meteor.*, **114**, 367–387, https://doi.org/10.1007/s10546-004-0857-1.

Rheinwalt, A., N. Marwan, J. Kurths, P. Werner, and F.-W. Gerstengarbe, 2012: Boundary effects in network measures of spatially embedded networks. *Europhys. Lett.*, **100**, 28002, https://doi.org/10.1209/0295-5075/100/28002.

——, N. Boers, N. Marwan, J. Kurths, P. Hoffmann, F.-W. Gerstengarbe, and P. Werner, 2016: Non-linear time series analysis of precipitation events using regional climate networks for Germany. *Climate Dyn.*, **46**, 1065–1074, https://doi.org/10.1007/s00382-015-2632-z.

Sanders, F., and E. Kessler, 1999: Frontal analysis in the light of abrupt temperature changes in a shallow valley. *Mon. Wea. Rev.*, **127**, 1125–1133, https://doi.org/10.1175/1520-0493(1999)127<1125:FAITLO>2.0.CO;2.

Smith, R. K., M. J. Redder, N. J. Tapper, and D. R. Christie, 1995: Central Australian cold fronts. *Mon. Wea. Rev.*, **123**, 16–38, https://doi.org/10.1175/1520-0493(1995)123<0016:CACF>2.0.CO;2.

Sun, J., and Coauthors, 2002: Intermittent turbulence associated with a density current passage in the stable boundary layer. *Bound.-Layer Meteor.*, **105**, 199–219, https://doi.org/10.1023/A:1019969131774.

——, and Coauthors, 2004: Atmospheric disturbances that generate intermittent turbulence in nocturnal boundary layers. *Bound.-Layer Meteor.*, **110**, 255–279, https://doi.org/10.1023/A:1026097926169.

——, L. Mahrt, R. M. Banta, and Y. L. Pichugina, 2012: Turbulence regimes and turbulence intermittency in the stable boundary layer during CASES-99. *J. Atmos. Sci.*, **69**, 338–351, https://doi.org/10.1175/JAS-D-11-082.1.

——, ——, C. Nappo, and D. H. Lenschow, 2015a: Wind and temperature oscillations generated by wave–turbulence interactions in the stably stratified boundary layer. *J. Atmos. Sci.*, **72**, 1484–1503, https://doi.org/10.1175/JAS-D-14-0129.1.

——, and Coauthors, 2015b: Review of wave-turbulence interactions in the stable atmospheric boundary layer. *Rev. Geophys.*, **53**, 956–993, https://doi.org/10.1002/2015RG000487.

Thomas, C. K., 2011: Variability of sub-canopy flow, temperature, and horizontal advection in moderately complex terrain. *Bound.-Layer Meteor.*, **139**, 61–81, https://doi.org/10.1007/s10546-010-9578-9.

——, A. M. Kennedy, J. S. Selker, A. Moretti, M. H. Schroth, A. R. Smoot, N. B. Tufillaro, and M. J. Zeeman, 2012: High-resolution fibre-optic temperature sensing: a new tool to study the two-dimensional structure of atmospheric surface-layer flow. *Bound.-Layer Meteor.*, **142**, 177–192, https://doi.org/10.1007/s10546-011-9672-7.

Van de Wiel, B. J. H., R. J. Ronda, A. F. Moene, H. A. R. D. Bruin, and A. A. M. Holtslag, 2002: Intermittent turbulence and oscillations in the stable boundary layer over land. Part I: A bulk model. *J. Atmos. Sci.*, **59**, 942–958, https://doi.org/10.1175/1520-0469(2002)059<0942:ITAOIT>2.0.CO;2.

——, A. F. Moene, O. K. Hartogensis, H. A. R. D. Bruin, and A. A. M. Holtslag, 2003: Intermittent turbulence in the stable boundary layer over land. Part III: A classification for observations during CASES-99. *J. Atmos. Sci.*, **60**, 2509–2522, https://doi.org/10.1175/1520-0469(2003)060<2509:ITITSB>2.0.CO;2.

van Hooijdonk, I. G. S., J. M. M. Donda, H. J. H. C. F. C. Bosveld, and B. J. H. van de Wiel, 2015: Shear capacity as prognostic for nocturnal boundary layer regimes. *J. Atmos. Sci.*, **72**, 1518–1532, https://doi.org/10.1175/JAS-D-14-0140.1.

——, and Coauthors, 2017: Near-surface temperature inversion growth rate during the onset of the stable boundary layer. *J. Atmos. Sci.*, **74**, 3433–3449, https://doi.org/10.1175/JAS-D-17-0084.1.

Vercauteren, N., and R. Klein, 2015: A clustering method to characterize intermittent bursts of turbulence and interaction with submesomotions in the stable boundary layer. *J. Atmos. Sci.*, **72**, 1504–1517, https://doi.org/10.1175/JAS-D-14-0115.1.

——, L. Mahrt, and R. Klein, 2016: Investigation of interactions between scales of motion in the stable boundary layer. *Quart. J. Roy. Meteor. Soc.*, **142**, 2424–2433, https://doi.org/10.1002/qj.2835.

Vignon, E., and Coauthors, 2017: Stable boundary-layer regimes at Dome C, Antarctica: observation and analysis. *Quart. J. Roy. Meteor. Soc.*, **143**, 1241–1253, https://doi.org/10.1002/qj.2998.

Weaver, A., and E. Wiebe, 2006: Micro meteorological network in greater Victoria schools: www.victoriaweather.ca. *CMOS Bull.*, **34**, 184–190.

White, L. D., 2009: Sudden nocturnal warming events in Mississippi. *J. Appl. Meteor. Climatol.*, **48**, 758–775, https://doi.org/10.1175/2008JAMC1971.1.

Zeeman, M. J., J. S. Selker, and C. K. Thomas, 2015: Near-surface motion in the nocturnal, stable boundary layer observed with fibre-optic distributed temperature sensing. *Bound.-Layer Meteor.*, **154**, 189–205, https://doi.org/10.1007/s10546-014-9972-9.